A Genetic Model Therapy Proposes a Critical Role for Liver Dysfunction in Mitochondrial Biology and Disease

Ankit Sabharwal[1*], Mark D. Wishman[1*], Roberto Lopez Cervera[1*], MaKayla R. Serres[1], Jennifer L. Anderson[2], Anthony J. Treichel[1], Noriko Ichino[1], Weibin Liu[1,3], Jingchun Yang[1,3], Yonghe Ding[1,3], Yun Deng[1,3,4], Steven A. Farber[2], Karl J. Clark[1], Xiaolei Xu[1,3], Stephen C. Ekker[1#]

[1]Department of Biochemistry and Molecular Biology, Mayo Clinic College of Medicine, Rochester, MN, United States of America; [2]Carnegie Institution for Science, Department of Embryology, Baltimore, Maryland, USA; [3]Division of Cardiovascular Diseases, Department of Medicine, Mayo Clinic College of Medicine, Rochester, MN, United States of America; [4]Present address: Department of Genetics and Development Biology, College of Life Sciences, Hunan Normal University, P.R. China

[*]Equal Contributions

#Corresponding Author: Stephen C. Ekker- Ekker.Stephen@mayo.edu

Abstract

The clinical and largely unpredictable heterogeneity of phenotypes in patients with mitochondrial disorders demonstrates the ongoing challenges in the understanding of this semi-autonomous organelle in biology and disease. Here we present a new animal model that recapitulates key components of Leigh Syndrome, French Canadian Type (LSFC), a mitochondrial disorder that includes diagnostic liver dysfunction. LSFC is caused by allelic variations in the Leucine Rich Pentatricopeptide repeat-containing motif (*LRPPRC*) gene. *LRPPRC* has native functions related to mitochondrial mRNA polyadenylation and translation as well as a role in gluconeogenesis. We used the Gene-Breaking Transposon (GBT) cassette to create a revertible, insertional mutant zebrafish line in the *LRPPRC* gene. *lrpprc* zebrafish homozygous mutants displayed impaired muscle development, liver function and lowered levels of mtDNA transcripts and are lethal by 12dpf, all outcomes similar to clinical phenotypes observed in patients. Investigations using an *in vivo* lipidomics approach demonstrated accumulation of non-polar lipids in these animals. Transcript profiling of the mutants revealed dysregulation of clinically important nuclearly encoded and mitochondrial transcripts. Using engineered liver-specific rescue as a genetic model therapy, we demonstrate survival past the initial larval lethality, as well as restored normal gut development, mitochondrial morphology

31 and triglyceride levels functionally demonstrating a critical role for the liver in the
32 pathophysiology of this model of mitochondrial disease. Understanding the molecular
33 mechanism of the liver-mediated genetic rescue underscores the potential to improve the clinical
34 diagnostic and therapeutic developments for patients suffering from these devastating disorders.

Introduction

The mitochondrion is a complex and essential organelle whose dysfunction is linked to a panoply of diverse human pathologies and diseases. The understanding of the traditional role of mitochondria as the powerhouses of the cell has evolved as the many roles in cellular and physiological homeostasis have been functionally enumerated far beyond this commonly known role in energy production via the electron transport chain (ETC). Today, mitochondria are known to directly contribute to calcium signaling, apoptosis, iron homeostasis, lipid metabolism, ATP-metabolism, immunity, and a host of other critical biochemical synthesis pathways (Green, 1998; Rizzuto et al., 2009; Spinelli and Haigis, 2018; Tiku et al., 2020; Valero, 2014). All of these cellular functions rely on well-orchestrated cross-talk between the nuclear and mitochondrial genome. Genetic lesions arising in the nuclear and/or mitochondrial genome can lead to mitochondrial dysfunction that present in humans with heterogeneous groups of clinical manifestations that differentially impact every organ system in the body (Chinnery et al., 2012; Vafai and Mootha, 2012). The widespread activity of mitochondria provides ample opportunities for mitochondrial dysfunction to play a role in human disease, but current understanding does not provide specificity in differential biological function or capacity in accurately predicting pathogenic details suitable for therapeutic development.

Mitochondrial disease can arise directly such as pathogenic genetic variations in mitochondrial DNA such as Mitochondrial Encephalopathy Lactic acidosis and Stroke (MELAS) or nuclear DNA including Leigh Syndrome, or as a secondary condition associated with an underlying pathology such as Alzheimer's disease, diabetes, or cancer (Moraes et al., 1992; Newsholme et al., 2012; Rahman et al., 1996; Urrutia et al., 2014; Wallace, 2012). Even in these circumstances where the proximal cause of disease initiation is known, the specific manifestations of mitochondrial dysfunction can produce a wide spectrum of clinical features that vary in severity and tissue specificity, even within patients harboring identical genetic variations (Gorman et al., 2016; McFarland et al., 2010). Therefore, establishing causality between phenotypes and genetic variations for a given mitochondrial disease is often challenging in a clinical setting.

Here we focus on Leigh Syndrome, French Canadian Type (LSFC), a well-defined mitochondrial disease with onset in infancy that manifests with diagnostic liver dysfunction. LSFC is a monogenic, autosomal recessive condition. LSFC was first discovered in the Saguenay-Lac-

65 Saint-Jean region of Quebec, Canada, where roughly 1 in 23 individuals was found to be a
66 carrier of a diseased allele (Morin et al., 1993). The most common allelic variant is due to an
67 A354V transition in exon 9 of the leucine rich pentatricopeptide repeat containing motif
68 (*LRPPRC*) protein, a nuclear-encoded gene. Other pathogenic variants in *LRPPRC* have been
69 reported in patients, including an 8 base pair deletion in exon 35 (Mootha et al., 2003) that
70 presents with reduced phenotypes compared to the A354V mutation. Patients with mutations in
71 *LRPPRC* experience a diverse array of clinical features centered around cytochrome oxidase
72 (COX) deficiency. These can include an early onset of hepatic microvesicular steatosis and
73 chronic lactic acidosis as neonates. Individuals born with LSFC have an average lifespan of less
74 than 5 years of age with most succumbing to a series of extreme, acute metabolic crises. Patients
75 that make it past the early life crises show a lessened disease state characterized by hypotonia,
76 language and mobility deficits and delays, and muscle weakness (Debray et al., 2011; Morin et
77 al., 1993). *LRPPRC* has also been implicated in other diseases such as neurofibromatosis,
78 Parkinson's disease, and viral infections such as HIV-1 (Cui et al., 2019).

79 LRPPRC belongs to the pentatricopeptide repeat (PPR) containing motif family of proteins.
80 Pentatricopeptide Repeats (PPRs) are non-catalytic RNA binding domains. PPR proteins consist
81 of a series of ~35 amino acid repeats wherein two hypervariable residues, those in the 5th and
82 35th position of the repeat, direct the binding of each repeat region to a single specific
83 ribonucleotide (Manna, 2015). The LRPPRC protein in humans has 20 annotated PPR domains
84 and is promiscuous, preferentially binding to different mitochondrial RNAs (Figure 1A). The
85 gene also has tetratricopeptide (TPR)- and HEAT (huntingtin-elongation A subunit-TOR)-like
86 tandem repeat sequences. The N terminus consists of multiple copies of leucine rich nuclear
87 transport signals, four copies of the transcriptional co-regulator signature LXXLL and PPR
88 motifs extending through the C terminus. The C terminus of the protein also consists of ENTH
89 (Epsin1 N-Terminal Homology) involved in cytoskeletal organization, vesicular trafficking,
90 DUF (Domain of Unknown Function) 28 and SEC1 domain for vesicular transport. *LRPPRC*
91 plays roles in the regulation of both nuclear and mitochondrial RNA expression at the
92 transcriptional and post transcriptional level (Liu and McKeehan, 2002; Mili and Piñol-Roma,
93 2003).

94 The majority of the protein is imported to mitochondria, where it forms a complex with the
95 steroid receptor RNA activator stem-loop (*SLIRP*) protein in the mitochondrial matrix. The

96 absence of *LRPPRC* leads to oligoadenylation of the transcripts. Studies using shRNAs to
97 knockdown *LRPPRC* in MCH58 human fibroblasts showed decreased transcript levels of genes
98 encoded on the mitochondrial chromosome (Gohil et al., 2010). *LRPPRC-SLIRP* is also
99 observed to relax RNA structure, making the 5' end of the mRNA accessible for the
100 mitochondrial ribosome to initiate translation (Cui et al., 2019). Loss of functional *lrpprc* in *C.*
101 *elegans* and mice revealed defects in mitochondrial biogenesis, decreased complex 1 and
102 cytochrome c oxidase activity, decreased stability of mitochondrial mRNAs, and dysregulated
103 mitochondrial translation (Cuillerier et al., 2017; Kohler et al., 2015; Xu et al., 2012).

104 Given that onset of LSFC is marked by the neurological and metabolic crisis (Morin et al., 1993)
105 and the liver is the major metabolic factory of the cell, therefore, the role of liver impairment in
106 LSFC represents a unique aspect of mitochondrial disease unseen in traditional Leigh syndrome.
107 Mice harboring liver-specific inactivation of *Lrpprc* displayed manifestations similar to LSFC
108 patients marked by mitochondrial hepatopathy, growth delay and reduced fatty acid oxidation
109 compared to controls. These animals also exhibited impaired cytochrome c oxidase and ATP
110 synthase activity along with increased susceptibility to calcium-induced permeability transition
111 (Cuillerier et al., 2017). Recently, a lipidomic profile study on LSFC patients highlighted a novel
112 role of this protein in the peroxisomal lipid metabolism (Ruiz et al., 2019).

113 Current diagnosis of LSFC hinges on measuring lactate levels in the blood and brain,
114 cytochrome C oxidase (COX) activity in patient fibroblasts, and sequencing of the *LRPPRC* gene
115 for mutations (Debray et al., 2011). The lack of a cure or effective therapies for LSFC patients
116 means that current clinicians must shift their focus to relieving and controlling symptoms. Focus
117 on dietary restrictions and lifestyle changes, including exercise and infection risk management,
118 are made to reduce the physiological and metabolic stress on the patient. To build upon a
119 heuristic paradigm for therapeutic interventions for these classes of disorders, we need to
120 establish disease models that serve as a suitable substrate to recapitulate the key functional
121 tissue-specific pathology of the disease.

122 As a model organism, zebrafish (*Danio rerio*) offers various advantages such as a short breeding
123 cycle, high fecundity, ex utero development, optically clear embryogenesis, rapid development
124 of internal organs, and easy maintenance (Lieschke and Currie, 2007). Zebrafish are a powerful
125 potential vertebrate model organism to study human mitochondrial disorders because of the

126 conserved mitochondrial genome and mitochondrial genetic machinery, as compared to its
127 human counterpart. The zebrafish and human mitochondrial genomes display ~65% sequence
128 identity at nucleotide level, and share the same codon usage, strand specific nucleotide bias and
129 gene order (Broughton et al., 2001; Sabharwal et al., 2019a). Recently, the zebrafish model has
130 shed light on mitochondrial disorders and helped expand our understanding of the mechanisms
131 of mitochondrial -associated pathology (Byrnes et al., 2018; Flinn et al., 2009; Plucińska et al.,
132 2012; Song et al., 2009; Steele et al., 2014).

133 We employed an insertional mutagenesis screen using the gene-breaking transposon (GBT)
134 (Clark et al., 2011) to model LSFC. The GBT construct is incorporated into the intron of an
135 endogenous gene via Tol2 transposase and uses a splice acceptor site to create a fusion protein
136 between the native transcript and a monomeric red fluorescent protein (mRFP) gene that contains
137 a transcription termination site (Fig 1B). When inserted intergenically, this result in translation of
138 a truncated endogenous gene product fused to mRFP. This enables spatiotemporal tracking of the
139 trapped gene's natural protein expression in real time. This insertion is reversible due to two loxP
140 sites located near each terminal repeat that enables removal of the GBT cassette using Cre
141 recombinase. The revertible nature of this construct allows for reversion of the mutant back to
142 wild type alleles to allow for tissue-specific or ubiquitous rescue of the mutated gene (Clark et
143 al., 2011; Ichino et al., 2019).

144 We describe here the first revertible zebrafish mutant with a single disruptive insertion in the
145 *lrpprc* gene to model LSFC. *lrpprc* homozygous mutants mimic many hallmarks observed in
146 patients such as early lethality, defective muscle development and decreases in mitochondrial
147 transcript levels. In addition, altered dietary lipid metabolism along with mitochondrial
148 dysmorphology was also observed in these mutants. A key outcome of this study is the reversion
149 of the LSFC-associated phenotype and survival using liver-specific Cre recombinase in the
150 homozygous *lrpprc* mutants, demonstrating a critical role of this organ is the pathogenesis of
151 disease in this animal model. This result contributes a novel paradigm towards identification of
152 therapeutic approaches for LSFC and for other related disorders.

153 # Methods

154 **Zebrafish handling and husbandry**

155 All adult zebrafish and embryos were maintained according to the guidelines established by
156 Mayo Clinic Institutional Animal Care and Use Committee (Mayo IACUC) (IACUC number:
157 A34513-13-R16).

158 **Mutant generation**

159 The GBT0235 allele was generated by injecting the pGBT-RP2.1 cassette as described to create
160 the *in vivo* protein trap lines (Clark et al., 2011; Ichino et al., 2019). Generation of these
161 transgenic fish lines involved microinjection of the vector DNA together with the transposase
162 RNA (Tol2) in single cell zebrafish embryos, followed by screening of the injected animals for
163 GFP and RFP expressions. To generate the larvae for liver-specific rescue data, non-GBT
164 transgenic marker lines carrying liver-specific Cre recombinase *Tg(−2.8fabp10:Cre;*
165 *−0.8cryaa:Venus)*^{S955} were used. *Tg(MLS: EGFP)* transgenic line was used to generate larvae to
166 study the subcellular localization of the truncated fusion protein.

167 **Zebrafish embryo genotyping (ZEG) protocol**

168 Deficiency of LRPPRC in humans shows an early neonatal phenotype, necessitating the ability
169 to investigate GBT0235 mutants at early stages of life. Likewise, our *lrpprc*$^{GBT0235/GBT0235}$
170 mutants exhibit lethality starting around 8 dpf. We needed the ability to genotype larvae at a
171 young age without sacrificing to enable experiments to be efficiently conducted on living
172 animals such as the survival assays and HPLC lipid analysis. An automated genotyping device
173 was employed for the rapid cellular extraction of DNA from zebrafish embryos (Lambert et al.,
174 2018). Larvae at 3 days post fertilization (dpf) were rinsed three times in fresh embryo water and
175 transferred to a new petri dish. Larvae were aspirated in 12 µL of embryo media and placed on
176 extraction chips in individual wells. An evaporation cover was attached, and the larvae were
177 agitated using a vibrating motor that was powered with 2.4V for 10 minutes. Immediately
178 following the vibration period, the samples were removed from the chip and placed into strip
179 tubes for storage. Larvae were replenished with embryo water and individually transferred to a
180 24 well plate for storage at 28°C. The collected sample was used as a template for PCR
181 amplification for genotyping of the larvae. Two PCR reactions were run using the same thermal

182 cycler conditions. The first consisted of 5 µL of 5x MyTaq Red PCR Buffer, 1 µL of 10µM
183 GBT0235ex22 FP2, 1 µL of 10µM GBT0235 WT RP, 0.25 µL of MyTaq DNA Polymerase, 3.5
184 µL of template, and 14.75 µL dH2O. The second PCR setup replaced the 10µM GBT0235 WT
185 RP with RLC_mRFP R1. Samples were run in a thermal cycler with following PCR conditions:
186 (1) 95°C, 5 min; (2) 95°C, 1 min; (3) 61.3°C, 30 sec; (4) 72°C, 1 min; (5) Go to step 2 39X; (6)
187 72°C, 5 min; (7) 12°C, hold. Samples were run on a 1% agarose gel and analyzed. We tested our
188 locus-specific *lrpprc* primers (Supplementary Table 1) and found successful amplification of
189 both our $lrpprc^{+/+}$ and $lrpprc^{GBT0235/GBT0235}$ bands.

190 **Genotyping of zebrafish larvae by fin clipping**

191 This larval genotyping protocol was adapted from previously described study (Wilkinson et al.,
192 2017). Larvae were placed in a petri dish containing 3 µL of 20% Tween per 30 mL of embryo
193 media. Larvae were individually placed on an inverted petri dish under a dissecting scope using
194 trans-illumination. A scalpel was used to cut the tail distal to the blood flow. The fin clip was
195 removed from the solution using forceps and placed into a PCR strip tube containing 10 µL of 50
196 mM NaOH. Scalpel and forceps were sterilized with an ethanol wipe between biopsies. Larvae
197 were transferred into a petri dish with fresh embryo media before being moved to a 24-well plate
198 for recovery while genotyping was performed. Tail biopsies were capped and heated to 98°C for
199 10 minutes and then cooled to 25°C. 10µL of 100mM Tris pH8 was added to each tube and
200 mixed. These samples were then used for PCR amplification. Following genotyping, embryos
201 were grouped by genotype and placed in petri dishes until needed for experiments.

202 **Capturing the spatio-temporal expression dynamics in the *in vivo* protein trap lines**

203 Larvae were treated with 0.2 mM phenylthiocarbamide (PTU) at 24 hours post fertilization (hpf)
204 to prevent pigmentation. Fish were anesthetized with 1X tricaine and mounted in 1.5% agarose
205 (Fisher Scientific, USA) prepared with 1X tricaine solution (0.18 mg/L) in an agarose column in
206 the imaging chamber. For Lightsheet microscopy, larval zebrafish were anesthetized with 1X
207 tricaine in embryo water during imaging procedure. RFP expression patterns of 6 dpf larval
208 zebrafish were captured using LP 560 nm filter as excitation and LP 585nm as emission using a
209 Lightsheet Z.1 microscope (Zeiss, Germany) 5X/0.16 NA dry objective. Confocal microscopy
210 was carried out embedding the 6 dpf larvae in 1 % (w/v in E2 medium containing tricaine) low-
211 melting agarose (Fisher Scientific, USA) in a 50-mm glass bottom dish (MatTek, USA). Once

212 the agarose set, it was immersed in E2 medium containing tricaine to prevent drying. Each set of
213 brightfield and RFP images for both heterozygous and homozygous mutants were acquired using
214 Zeiss LSM780 (40XW/1.2 NA) and the images shown are the maximum image projections of
215 the z-stacks obtained from each direction.

216 **Colocalization analysis**

217 *lrpprc*$^{GBT0235/+}$ adult zebrafish were out-crossed to *Tg(MLS: EGFP)* zebrafish (Kim et al., 2008;
218 Sabharwal et al., 2019b) to obtain *Tg(MLS:EGFP) lrpprc* $^{GBT0235/+}$. Embryos were maintained in
219 0.2 mM phenylthiocarbamide from 24 hpf and anesthetized with tricaine (0.18 mg/L). Larvae
220 sample preparation was done as described above. The 2 dpf larvae were viewed under a Zeiss
221 LSM780 confocal microscope. Laterally oriented Z-stacks of representative images of the caudal
222 fin for GFP and mRFP expressions were captured using the laser with Ex488 and Ex561,
223 respectively under a 63XW/1.2 NA water objective. Each set of images were independently
224 acquired at different fluorescent wavelengths and a composite image was generated using Zeiss
225 Zen microscope software.

226 **Survival assay**

227 *lrpprc* $^{GBT0235/+}$ adult zebrafish were crossed with *Tg(−2.8fabp10:Cre; −0.8cryaa:Venus)*^{S955} to
228 obtain double transgenic adult zebrafish expressing both the GBT cassette and the fabp10 driven
229 Cre recombinase (liver rescued). At 5 dpf the larval zebrafish were anesthetized using 1X
230 tricaine (0.18 mg/L) and screened for RFP fluorescence and gamma crystalline Venus (V) and
231 sorted. The resultant groups were {RFP-,V- (*lrpprc*$^{+/+}$), {RFP-,V+ (*lrpprc*$^{+/+}$, liver (fabp10-cre)
232 rescued)}, {RFP+,V+ (*lrpprc*$^{GBT0235/+}$ and *lrpprc*$^{GBT0235/GBT0235}$, liver (fabp10-cre) rescued)},
233 {RFP+,V-, BL+(*lrpprc*$^{GBT0235/GBT0235}$)}, {RFP+,V-, BL-(*lrpprc*$^{GBT0235/+}$). At 5 dpf, the RFP+/V-
234 group was anesthetized and sorted based on the presence of darkened liver (DL) phenotype on a
235 brightfield microscope. The resultant groups were R+/V-/DL+ and R+/V-/DL-. It is assumed at
236 this point that the R+/V- BL+ larvae are the GBT0235 (*lrpprc*) homozygous offspring and the
237 R+/V- BL- larvae are the GBT0235 heterozygous offspring, based on phenotypic
238 characterization of homozygous GBT0235 larval zebrafish. The above-mentioned groups were
239 placed on the Mayo Clinic Zebrafish Facility at 6 dpf. Live counts were recorded daily from 6
240 dpf to 12 dpf. At the end point (12 dpf) the remaining larvae from each group were counted and

241 euthanized for genotyping using NaOH extraction followed by PCR using primers listed in
242 Supplementary Table 1.

243 **RNA extraction and sample preparation**

244 *lrpprc* $^{GBT0235/+}$ adult zebrafish were incrossed and embryos collected and placed in a 28°C
245 incubator until larvae were ready for RNA isolation. Larvae were sorted for RFP expression on 6
246 dpf and separated into dishes. RNA isolation was performed using trizol extraction. Briefly,
247 larvae were placed in 500 µL of trizol and homogenized using a handheld homogenizer on ice
248 and then incubated at room temperature for 5 minutes. Chloroform was added followed by a 15-
249 minute incubation on ice before spinning in tabletop centrifuge at 4°C for 15 minutes. The
250 aqueous layer was removed and placed into a separate 1.7mL centrifuge tube, some of which
251 was used to genotype the larvae. The remainder was put through a series of ethanol and DNase I
252 treatments to isolate and purify the RNA. Each embryo was genotyped using the *lrpprc* ex22_F,
253 GBT0235_R1, and mRFP R1 and RNA samples were grouped according to genotype. RNA
254 quantity and quality were assured to meet the standards of the Genewiz RNA-sequencing
255 platform using the spectrophotometer.

256 **Mitochondrial DNA relative gene expression analysis**

257 Adult *lrpprc*$^{GBT0235/+}$ zebrafish were mated and embryos were collected. Larvae were analyzed
258 for RFP expression and darkened liver (DL) phenotype at 6 dpf. RFP positive, DL positive fish
259 were used as the experimental group to measure mtDNA transcript expression against RFP
260 negative, DL negative embryos as a control. For each clutch, 3 fish from each condition were
261 sorted for RNA extraction. After initial sorting, individual larvae were placed in a 1.7mL tube
262 with 350 µL of RLT buffer: BME at 100:1. Embryos were then homogenized using ~30 steel
263 beads and tissuelyzed at max frequency for 5 minutes. Homogenized samples were then added to
264 Maxtract tubes, carefully avoiding the steel beads and a phenol/chloroform preparation was used
265 to separate out nucleic acid material. RNA was then isolated and purified using the RNeasy
266 Micro Kit (Qiagen, USA) according to manufacturer's specifications and spectrophotometry was
267 performed for sample quantification. 250 ng of RNA per fish was used for reverse-transcription
268 into cDNA using the Thermo Fisher SuperScript II kit (Thermo Fisher Scientific, USA).
269 Requisite no reverse transcriptase (RT) controls were run parallel to test for genomic DNA
270 contamination. cDNA was diluted 16-fold with deionized water and amplified using the

271 SensiFAST SYBR Lo-ROX kit (Bioline, USA) for qRT-PCR analysis. Each sample was run in
272 triplicate for RT conditions and duplicate for NRT conditions. Process was repeated for four
273 individual clutches of GBT0235 embryos. Wild type and mutant transcripts levels were
274 normalized to eukaryotic translation elongation factor 1 alpha 1, like 1(*eef1a1l1*).

275 **Birefringence assay**

276 *lrpprc*$^{GBT0235/+}$ adult zebrafish were in-crossed to obtain a population of *lrpprc*$^{+/+}$, *lrpprc*$^{GBT0235/+}$,
277 and *lrpprc*$^{GBT0235/GBT0235}$ offspring. Embryos & larvae were maintained in E2 embryo medium at
278 28.5°C at a density of 30 per dish and kept on a 14-hour light/10-hour dark cycle. At ~96 hours
279 post-fertilization, 12 larvae per parental pair were anesthetized with tricaine (0.18 mg/L) and
280 embedded as described in the previous section. The larvae were viewed using a Stemi SV11
281 stereomicroscope (Zeiss, Germany) equipped with a polarized lens underneath the stage and
282 polarized lens on the objective lens. The polarized lens on the objective was rotated until the
283 background went dark. Birefringence images were then acquired using a DSLR camera (Canon,
284 Powershot G10) in RAW mode using an ISO of 200, aperture of f/4.5, and an exposure of 1/15 s.
285 Larvae were subsequently rescued from agarose using ultra-fine forceps, placed into 8-strip
286 tubes, euthanized by tricaine overdose, and lysed for DNA extraction using 30 µL of 50 mM
287 NaOH (incubated at 95°C for 25 minutes, then neutralized with 3 µL of 1 M Tris-HCl (pH = 8)).
288 This neutralized lysate was used for PCR genotyping.

289 RAW images were converted to 8-bit grayscale TIFFs in Adobe Photoshop. Grayscale TIFF
290 birefringence images were imported into NIH ImageJ/FIJI for further analysis. We outlined an
291 area in each individual fish that corresponded to the birefringence from its body using the wand
292 tool (legacy mode, threshold = 16). The birefringence signal from the otolith was specifically
293 excluded from these measurements. All outlined regions were saved as regions of interest
294 (ROIs). Within these ROIs, measurements for area, mean gray value, min gray value, max gray
295 value, and integrated gray value density were obtained. During data collection and analysis,
296 experimenters were blind to the genotype and RFP expression pattern of the larvae. After un-
297 masking the data, area, mean gray value, and integrated gray value density were utilized to make
298 plots and assessed for statistical differences between *lrpprc*$^{+/+}$ and *lrpprc*$^{GBT0235/GBT0235}$ animals.
299 Each individual data point represents a single animal. Each parental pair represents a biological
300 replicate. This dataset contains five biological replicates from two separate days.

301 **RNA sequencing and analyses**

302 RNA library preparations and sequencing reactions were performed at GENEWIZ, LLC. (South
303 Plainfield, NJ, USA). Quantification of RNA samples was carried out using Qubit 2.0
304 Fluorometer (Thermo Fisher Scientific, USA) and further, the RNA integrity was checked using
305 Agilent Tapestation 4200 (Agilent Technologies, USA). RNA sequencing libraries were
306 prepared using the NEB Next Ultra RNA Library Prep Kit for Illumina using manufacturer's
307 instructions (NEB, USA). Briefly, mRNAs were initially enriched with oligo(dT)
308 beads. Enriched mRNAs were fragmented for 15 minutes at 94°C. Subsequently, cDNA
309 fragments were synthesised, end repaired and adenylated at 3'ends, and universal adapters were
310 ligated to them, followed by index addition and library enrichment by PCR with limited cycles.
311 The sequencing library was validated on the Agilent TapeStation (Agilent Technologies, USA),
312 and quantified by using Qubit 2.0 Fluorometer (Thermo Fisher Scientific, USA) as well as by
313 quantitative PCR (KAPA Biosystems, USA). The sequencing libraries were clustered on a single
314 lane of a flow cell. After clustering, the flowcell was loaded on the Illumina HiSeq4000
315 instrument according to manufacturer's instructions. The samples were sequenced using a
316 2x150bp Paired End (PE) configuration. Image analysis and base calling were conducted by the
317 HiSeq Control Software (HCS). Raw sequence data (.bcl files) generated from Illumina HiSeq
318 was converted into fastq files and de-multiplexed using Illumina's bcl2fastq 2.17 software. One
319 mismatch was allowed for index sequence identification.

320 Paired-end reads of 150 bp length generated for the homozygous mutant and the wild type was
321 trimmed with a base quality cut off of Phred score Q30 using Trimmomatic (Bolger et al., 2014).
322 Filtered reads were pseudoaligned to the zebrafish reference genome Zv10 version. Kallisto
323 (Bray et al., 2016) was used for transcript assembly and calculation of relative expression values
324 across transcripts. Tximport (Soneson et al., 2015) was used to summarize transcript level counts
325 at gene level. Differential expression was computed using DESeq2 as counts per million (CPM)
326 (Love et al., 2014). Genes with a fold change of greater than $\log_2 0.5$ and less than $\log_2 0.5$ were
327 considered to be upregulated and downregulated respectively.

328 Human orthologs of differentially expressed zebrafish genes were identified from ZFIN
329 (Zebrafish Information Network) and Ensembl. Differentially expressed human orthologs of
330 zebrafish genes were run against the human Mitocarta database to identify upregulated and
331 downregulated mitochondrial genes involved in biological pathways resident in mitochondria

332 (Calvo et al., 2016). Differentially expressed genes were entered in the PANTHER (Mi et al.,
333 2019) database to identify the protein class and biological process of these genes. For the
334 differentially expressed genes, we predicted the enriched or depleted pathways by using a web
335 based integrated analysis platform, Genetrail2 (Stockel et al., 2016). Differentially expressed
336 genes along with their respective calculated scores were fed as the input file. Scores were
337 calculated as per the following formula: Score= {$-\log_{10}$(p-value) * $\log_2$fold change}.
338 Kolmogorov-Smirnov test was used as the statistical test for the gene set enrichment analysis to
339 find enriched/depleted biological pathways from the KEGG pathways, Reactome pathways and
340 Wiki pathways.

341 **Oil Red O staining**

342 For whole mount staining at the larval stage, 8 dpf larvae were fixed in 10% NBF overnight. The
343 Oil Red O staining procedures were followed as described previously (Kim et al., 2013). Briefly,
344 *lrpprc*$^{+/+}$, *lrpprc*$^{GBT0235/GBT0235}$ and *Tg(fabp10:Cre)lrprrc*$^{GBT0235/GBT0235}$ larvae were rinsed three
345 times (5 minutes each) with 1× PBS/0.5% Tween-20 (PBS-T). After removing PBS-T, larvae
346 were stained with a mixture of 300 µL of 0.5% ORO in 100% isopropyl alcohol and 200 µL of
347 distilled water for 15 minutes. Larvae were then rinsed with 1× PBS-Tween for three times,
348 twice in 60% isopropyl alcohol for 5 minutes each, briefly rinsed in PBS-Tween, fixed in 10%
349 NBF for 10 minutes, and then mounted in glycerol for imaging. All outlined regions were saved
350 as regions of interest (ROIs). Within these ROIs, measurements for area were obtained and plots
351 and statistical analyses were performed. Oil Red O images were captured with a color camera in
352 JPEG format. For analysis, all images were de-identified using the sample function in R
353 (https://www.r-project.org, https://rstudio.com). De-identified JPEG images were then imported
354 into NIH FIJI/ImageJ and converted from RGB color images to 8-bit grayscale images. For each
355 batch of images (corresponding to one day of experiments), an image with dark Oil Red O
356 staining and an image with light Oil Red O staining were respectively used to determine the
357 lower and upper gray values (the threshold) for positive staining. Briefly, the lower edge of the
358 threshold was set as the gray value that most pixels representing melanocytes were darker than,
359 but almost all dark Oil Red O staining was brighter than. Similarly, the upper edge of the
360 threshold was determined to be the gray value where most pixels representing the background
361 outside of the fish were brighter than, but some light Oil Red O staining was darker than. This
362 left a range of 40-45 gray values that encompassed the most Oil Red O staining. To quantify only

363 the Oil Red O staining in the liver, we drew a single region of interest that bordered the liver of
364 the most darkly stained larvae. This region of interest (ROI) specifically excluded the area
365 around the swim bladder due to accumulation of Oil Red O solution surrounding the swim
366 bladder in a majority of images. Within this ROI, the area of pixel values within the threshold in
367 each larva was determined using the "limit to threshold" option in the "set measurements" menu
368 in FIJI. After areas of Oil Red O staining were extracted from the images, they were re-identified
369 into three groups: *lrpprc*$^{+/+}$, *lrpprc*$^{GBT0235/GBT0235}$, and *Tg(fabp10:Cre)/lrpprc*$^{GBT0235/GBT0235}$.

370 **Electron microscopy of hepatocyte mitochondria and image analysis**

371 Wild-type, *lrpprc*$^{GBT0235/GBT0235}$, *and Tg(fabp10:Cre)/lrpprc*$^{GBT0235/GBT0235}$ zebrafish larvae were
372 fixed and imaged using transmission electron microscopy as described in the previous study
373 (Wilson et al., 2019). Briefly, 4 dpf embryos were fixed for 1 to 3 hours in a mixture of 3%
374 glutaraldehyde, 1% formaldehyde, and 0.1 M cacodylate. Embryos were embedded in 2% low
375 melt agarose followed by processing as described earlier (Zeituni et al., 2016). Following
376 embedding steps, post-fixation for 1 hour with 1% osmium tetroxide and 1.25% potassium
377 ferricyanide in cacodylate solution occurred. Larvae were rinsed twice with water and incubated
378 in 0.05 maleate pH 6.5 before staining overnight at 4°C in 0.5% uranyl acetate. Following
379 overnight incubation, samples were washed with water and dehydrated using ethanol dilution.
380 Samples were washed with propylene oxide and then incubated with propylene oxide/resin
381 followed by an overnight evaporation period. Finally, larvae were embedded in 100% resin at
382 55°C overnight and then 70°C for three days. Sectioning was performed on Reichert Ultracut-S
383 (Leica Microsystems, Germany), mounted on mesh grids, and stained with lead citrate. Images
384 were taken using a Phillips Technai-12 electron microscope and 794 Gatan multiscan CCD
385 camera. Images were scored for hepatocytes using classical hallmark of lipid droplets and
386 subsequently were de-identified and scored by genotype for mitochondrial morphology, in
387 particular the structure and integrity of mitochondrial cristae.

388 **Feeding of fluorescently tagged long-chain fatty acids**

389 Larvae were genotyped for number of copies (0, 1, or 2) of the RP2 insertion into the *lrpprc*
390 locus and presence or absence of the liver-specific CRE construct *(-2.8fabp10:Cre; -*
391 *0.8cryaa:Venus*). In each of four experiments, an equal number of 6 dpf larvae of each genotype
392 (18–24) was pooled and arrayed separately in Falcon brand 6-well tissue culture plates for

393 delivery of a fluorescently tagged long-chain fatty acid feed. 4,4-difluoro-5,7-dimethyl-4-bora-
394 3a,4a-diaza-*s*-indacene 3-dodecanoic acid (BODIPY^{TM} FL C12; Thermo Fisher Scientific, USA)
395 (4 µg/mL) was emulsified in a solution of 5% chicken egg yolk liposomes (in embryo medium)
396 as previously described (Carten et al., 2011). Since larvae can vary greatly in amount they ingest,
397 non-metabolizable TopFluor Cholesterol (conc, 23-(dipyrrometheneboron difluoride)-24-
398 norcholesterol; Avanti Lipids, USA) was added to the feed solution to serve as a readout of
399 amount ingested, allowing for normalization of the HPLC output. TopFluor Cholesterol is harder
400 to get into solution compared to BODIPY FL C12: embryo medium and 1% fatty acid-free BSA
401 was prewarmed to 30ºC. After 4 hours of feeding in a light-shielded shaking incubator (30ºC, 30
402 rpm), larvae were rinsed in fresh embryo media and screened for ingestion (darkened intestines)
403 under a stereomicroscope. Larvae that did not eat were disincluded from the study. Larvae that
404 ate were moved to tissue culture plates with fresh embryo media for an overnight chase period of
405 12.5 h in a 28.5°C light-cycling (14 h on, 10 h off) incubator. Pools of 8–13 larvae from each
406 group were snap frozen on dry ice in microcentrifuge tubes and stored dry at -80°C for lipid
407 extraction.

408 **Sample preparation and HPLC analyses of long-chain fatty acids**

409 Frozen samples of pooled larvae were subject to lipid extraction using a modified Bligh-Dyer
410 procedure. Extractions were dried and resuspended in 50 µL HPLC-grade isopropanol (HPLC
411 injection solvent). Sample components were separated and detected by an HPLC system as
412 described previously (Quinlivan et al., 2017). Chromatographic peak baselines were manually
413 delimited and peak areas were automatically measured (Chromeleon 7.2; Thermo Fisher
414 Scientific). Peak areas per larval equivalent were calculated and normalized to the TopFluor
415 Cholesterol peak (non-metabolizable; added to the fluorescent fatty acid feed). To fit a linear
416 model wherein the outcomes may have possible unknown correlations, generalized estimated
417 equations (gee) was performed on the R platform comparing total triglyceride area as well as
418 individual peaks/groups of peaks. Assessment of normality by visual examination of Q-Q
419 (quantile-quantile) plots confirmed that the standard normal curve is a valid approximation for
420 the distribution of the data. P-values were obtained from the standard normal Z-table.

421 **Statistical analyses**

422 Plots and statistical analyses including Man-Whitney U test, Sidak's multiple comparisons test,
423 student's t-test and construction of heat map were performed in GraphPad Prism 8 (GraphPad
424 software). Pearson's correlation coefficient and Manders split coefficients were used for pixel
425 intensity spatial correlation analysis using coloc2 plugin of Fiji image processing package.
426 Statistical significance was derived by Costes p test. Kolmogorov-Smirnov test was used as the
427 statistical test for the gene set enrichment analysis on GeneTrail2 webserver. Results of the
428 statistical analyses have been described either in the results section or in the figure legends.

429 ## Results

430 **Spatiotemporal expression dynamics of GBT0235 tagged by the *in vivo* protein trapping**

431 To generate and identify the *in vivo* protein trap mutant, a GBT mutagenesis screen was
432 conducted as described previously (Ichino et al., 2019). Briefly, genomic DNA and mRNA
433 expression analyses revealed that the *in vivo* protein trap line GBT0235 contained a single RP2.1
434 integration event within intron 22 (38 exons total) of the *lrpprc* gene on chromosome 13 (Figure
435 1B). The RP2.1 GBT protein trap cassette overrode the transcriptional splicing machinery of the
436 endogenous *lrpprc* gene, creating an in-frame fusion between the upstream endogenous exons
437 and the start codon-deficient mRFP reporter sequence. This mRFP-fusion resulted in a
438 translation product that was predicted to be truncated from 1461 amino acids to 793 amino
439 acids. RFP expression analysis of GBT0235 during zebrafish embryonic development revealed
440 onset of reporter expression as early as one cell stage that could be traced until late larval stages.
441 For instance, animals heterozygous for the GBT0235 allele (hereafter $lrpprc^{GBT023/5+}$) exhibit
442 ubiquitous RFP expression throughout the body at 6 dpf with strong expression in liver, gut and
443 muscles (Figure 2A). To estimate transcriptional effects of the GBT vector in GBT0235, qPCR
444 was carried out on the cDNA from homozygous mutants using primers spanning exon 22-23 of
445 the genomic locus—the site of insertion. Endogenous *lrpprc* transcript levels were negligible in
446 homozygous mutants, $lrpprc^{GBT0235/GBT0235}$, as compared to wild type controls, $lrpprc^{+/+}$,
447 indicating a nearly complete knockdown of the endogenous gene (Figure 2B).

448 ***lrpprc$^{GBT0235/+}$* mutants exhibit mitochondrial localization of Lrpprc-mRFP protein**

449 In humans *LRPPRC* is a nuclear-encoded gene that encodes for a protein that can be translocated
450 to the mitochondria (Siira et al., 2017; Sterky et al., 2010) where it is known to play an important
451 role in mitochondrial mRNA stability. To investigate the subcellular localization of the mRFP
452 fusion protein (the truncated Lrpprc tagged to mRFP), we crossed *lrpprc$^{GBT0235/+}$* to
453 *Tg(MLS:EGFP)* zebrafish. The *Tg(MLS:EGFP)* line served as a positive control wherein EGFP
454 is fused to the mitochondrial localization signal derived from the zebrafish ortholog of human
455 *COX8A* (Kim et al., 2008). Larvae from the outcross of *lrpprc$^{GBT0235/+}$* and *Tg(MLS:EGFP)* were
456 imaged at high magnification (63X) using confocal microscopy. The caudal fin of 2 dpf (Figure
457 2C) and myocytes (skeletal muscle region) of 4 dpf (Supplementary Figure 1) zebrafish embryos
458 were selected to observe the mitochondrial network. The caudal fin presents a unique advantage
459 of studying the mitochondrial sub-cellular network *in vivo* as it is as few as two cells thick.
460 Images were taken showing the reticular mitochondrial network marked by the GFP
461 (*Tg(MLS:EGFP)*) and the expression pattern of the Lrpprc-mRFP in skin cells. Resulting images
462 were overlaid to generate a composite image and revealed an overlap between the GFP and
463 Lrpprc-mRFP fusion protein in caudal fin in the zebrafish larvae (Figure 2C).

464 ***lrpprc$^{GBT0235/GBT0235}$* mutants develop hallmarks of LSFC**

465 Clinical presentations of patients with LSFC identify a number of hallmarks that we examined in
466 the *lrpprc$^{GBT0235/GBT0235}$* mutants. LSFC patients exhibit metabolic/acidotic crisis followed by
467 death within the first 2 years of life. We therefore hypothesized that our GBT protein trap allele
468 would lead to larval lethality in zebrafish. To assess the survivability, we examined the larvae
469 during the first 12 days of development and obtained a survival curve for the three genotypes
470 (*lrpprc$^{+/+}$, lrpprc$^{GBT0235/+}$, and lrpprc$^{GBT0235/GBT0235}$*). *lrpprc$^{GBT0235/GBT0235}$* homozygous mutants
471 had a similar survival percentage to that of heterozygous mutants and wild type through 6 dpf.
472 After 6 dpf, mortality was observed in the homozygous mutant group and resulted in 100%
473 lethality at the end of the follow-up on 12 dpf (Figure 3A). In contrast, the survival trend was
474 similar between the heterozygous mutants and the wild type animals. The mortality rate was thus
475 strongly affected by the *lrpprc$^{GBT0235/GBT0235}$* genotype. To assess the impaired function of the
476 *lrpprc* gene, we investigated the transcript levels of mitochondrial-encoded genes. qRT-PCR
477 analysis of these genes revealed a significant drop-off in transcript levels in the

478 *lrpprc*$^{GBT0235/GBT0235}$ mutants compared to wild type larvae (Figure 3B). Expression of nuclear
479 genes were found to be similar across the two genotypes. These findings are consistent with data
480 observed in the previous studies that have shown a crucial role for *lrpprc* in mitochondrial
481 mRNA stability.

482 Since onset of LSFC has multisystemic involvement, we further investigated for phenotypic
483 defects in tissues such as muscle and liver. Survivors of the early life metabolic crises associated
484 with LSFC often show skeletal muscle phenotypes including hypotonia, muscle weakness, and
485 mobility defects (Sasarman et al., 2015). To investigate whether our *lrpprc*$^{GBT0235/GBT0235}$ mutants
486 recapitulate this phenotype, we used birefringence—the refraction of plane polarized light
487 through a complex, ordered structure—as a readout of skeletal muscle development and structure
488 in 4 dpf larvae. *lrpprc*$^{GBT0235/GBT0235}$ larvae exemplified (Figure 4A and 4B) a decrease in
489 integrated density and mean gray value when compared with wild type siblings (Figure 4C-4E)
490 and, indicating a deficiency in muscle development specific to *lrpprc*$^{GBT0235/GBT0235}$ mutant
491 larvae.

492 ***lrpprc*$^{GBT0235/GBT0235}$ mutants display altered transcriptomic signature**

493 To assess genome wide transcriptional changes in *lrpprc*$^{GBT0235/GBT0235}$ mutants, strand specific
494 paired end RNA sequencing (Illumina, USA) with mean read length of 150 bp were generated
495 using HiSeq sequencing platform (Illumina, USA). Approximately 67 million reads were
496 generated for both the *lrpprc*$^{+/+}$ and *lrpprc*$^{GBT0235/GBT0235}$ RNA preparations. Approximately 88%
497 of the bases had a quality score of >30. The reads were aligned onto the Zv10 reference genome
498 after filtering low quality reads with cut-off Q30 using Trimmomatic software (Bolger et al.,
499 2014). Reads were pseudoaligned using kallisto (Bray et al., 2016) with an average mapping
500 percentage of 79.4%, and approximately 46.18% uniquely mapped reads, and were further
501 assembled across the genome to quantify transcript expression. Transcript level expression was
502 summarized at gene level using Tximport (Soneson et al., 2015). To compare quantitative
503 expression of genes across conditions, we performed differential expression analysis using
504 DESeq2 (Love et al., 2014). The number of transcripts obtained with CPM>1 is as follows:
505 19205 in WT and 20424 in *lrpprc* homozygous mutant respectively. Empirical cutoff of genes
506 with $\log_2$Fold Change >= 1 (p-value < 0.1) and $\log_2$Fold Change <= -1 (p-value < 0.1) were
507 shortlisted as upregulated and downregulated genes respectively (Figure 5A). 825 genes were

508 observed to be significantly upregulated and 776 genes were significantly downregulated in the
509 *lrpprc* homozygous mutants. The human Mitocarta2.0 catalog (Calvo et al., 2016) is a list of
510 1158 nuclear and mtDNA genes encoding for proteins localized in mitochondria. Overall, 30 and
511 44 human orthologs of zebrafish upregulated and downregulated genes, respectfully, overlapped
512 with the database (Figure 5B and Supplementary File 2).

513 Functional classification analysis of the differentially expressed genes using PANTHER (Mi et
514 al., 2019) was performed on two bases: protein class based on the biochemical property and the
515 other was biological process (Figure 5C and Supplementary File 3) in which a gene is involved
516 in the cellular niche. 11% and 12% of the upregulated genes were gene-specific transcriptional
517 regulator and metabolic interconversion enzymes, respectively. Other protein classes that were
518 majorly represented were nucleic acid binding proteins, transporter and protein modifying
519 enzymes. 28% and 16% of the downregulated genes fell in the category of protein class
520 belonging to metabolic interconversion enzyme and protein modifying enzymes. Other protein
521 classes that were majorly represented were translational protein, protein binding activity
522 modulator, nucleic acid binding proteins and gene-specific transcriptional regulator. Most of the
523 differential expressed genes were involved in biological processes such as metabolic process and
524 cellular process and biological regulation. Gene set enrichment analysis predicted mitochondrial
525 respiration and lipid metabolism pathways to be depleted in the *lrpprc*$^{GBT0235/GBT0235}$ mutants
526 (Supplementary File 4). These pathways followed a similar trend as observed by the expression
527 of mitochondrial encoded transcriptome and *lrpprc* transcript. Certain signaling pathways such
528 as MAPK signaling, JAK-Stat signaling were also found to be enriched in these animals.

529 **_lrpprc_$^{GBT0235/GBT0235}$ mutants show altered lipid metabolism**

530 Liver is a tissue that has high energetic demand and thus mitochondria are abundant in
531 hepatocytes. The spectrum of the expression of the Lrpprc-mRFP protein was well captured in
532 the liver of the heterozygous (Figure 6A) and homozygous zebrafish mutants (Figure 6B),
533 revealing visible hepatomegaly visible at the gross morphology level in larval animals.
534 Interestingly, *lrpprc*$^{GBT0235/GBT0235}$ mutants further display a darkened liver phenotype under
535 brightfield microscopy, reinforcing the involvement of the liver as distinguishing feature in
536 LSFC as compared to traditional Leigh Syndrome (Figure 6C). This hepatomegaly and higher
537 contrast liver phenotype were used as the basis to investigate what role might be played by the

538 liver in this disease. First, we used Oil Red O staining to investigate whether there was a change
539 in the distribution of lipids in *lrpprc*$^{GBT0235/GBT0235}$ mutants. We found increased lipid
540 accumulation in the livers of homozygous mutants (Figure 6E and 6G) compared to wild type
541 (Figure 6D and 6G), suggesting the observed darkened liver phenotype could be caused by a
542 change in the density of the stored lipids.

543 To ascertain the hepatic mitochondrial stress which leads to larval lethality (Figure 6H), electron
544 microscopy of the hepatocytes was conducted both for heterozygous and homozygous mutants.
545 Altered morphology of the mitochondria along with irregular shape and distribution of cristae
546 was observed in the hepatocytes of the *lrpprc* homozygous mutants (Figure 6I and 6J).

547 Since lipid metabolism is a basic liver function dependent on mitochondrial activity, and
548 disruption may lead to acute metabolic crises and death, we further examined how lipid profiles
549 are altered in the null mutants using earlier described methods (Quinlivan et al., 2017) Quinlivan
550 (2017). By coupling the feeding of a fluorescent fatty acid analog with high-performance liquid
551 chromatography methods, we asked whether the *lrpprc* null mutants have differences in fatty
552 acid metabolism compared to wildtype. For these experiments, we fed 6 dpf larvae for 4 hours in
553 a 5% chicken egg yolk solution containing a fluorescent long-chain fatty acid analog
554 (BODIPY™ FL C12) and a non-metabolizable fluorescent reagent (TopFluor® Cholesterol) to
555 assess and correct for amount ingested. After a 12.5-hour chase in fresh media, we extracted total
556 lipids and subjected them to HPLC with fluorescent detection. Extracted lipids were injected
557 across a nonpolar column which separates lipid species by solubility. While chromatograph peak
558 areas were lower overall in the homozygotes (Figure 7A), indicating less ingestion, the non-
559 metabolizable fluorescence allows us to correct for differences (Figure 7B). After chromatograph
560 peak areas were normalized to the non-metabolizable reagent, we found that the *lrpprc*$^{+/+}$,
561 *lrpprc*$^{GBT0235/+}$, and *lrpprc*$^{GBT0235/GBT0235}$ larvae channeled the dietary fluorescent FA into
562 cholesterol ester in similar levels, allowing for efficient cholesterol transport. However, we found
563 that the null mutants incorporated twice as much of the dietary fluorescent FA into non-polar
564 lipids compared to their wildtype siblings (*lrpprc*$^{GBT0235/GBT0235}$/*lrpprc*$^{+/+}$ = 2.040, 95% CI =
565 1.122–3.709, p= 0.019; (Figure 7C)).

566 We next asked whether any particular peak or peak cluster contributed to the higher levels of
567 incorporation into non-polar lipids in the homozygous mutants and found that three of four non-

568 polar lipid peaks or peak clusters are significantly higher (*lrpprc*$^{GBT0235/GBT0235}$/ *lrpprc*$^{+/+}$ for
569 peaks (1), (2), and (4), respectively = 1.73 [1.02–2.94], 1.99 [1.13–3.52], and 2.91 [1.47–5.79]; p
570 = 0.043, 0.017, and 0.002; Figure 7B). While we are unable to define the exact identities of these
571 peaks at this time, these are likely to be largely made of triacylglycerides and diacylglycerides,
572 the major components of nonpolar lipids along with cholesterol esters. The FA composition, as
573 detected by HPLC-CAD, did not differ between the groups (post-normalization for total lipid
574 levels).

575 **Liver-specific rescue reverses phenotypes seen in *lrpprc*$^{GBT0235/GBT0235}$ mutants**

576 The hepatic dysfunction seen in LSFC patients coupled with the lipid accumulation and darkened
577 liver phenotype in GBT0235 mutants pointed to the liver as an important potential therapeutic
578 avenue. The revertible nature of the GBT construct enables the organismal or tissue-specific
579 reversion to wild type by removal of the cassette via Cre recombinase. Therefore, by crossing
580 *lrpprc* mutants to *Tg(−2.8fabp10:Cre; −0.8cryaa:Venus)*^{S955} zebrafish, we were able to create a
581 liver-rescued *lrpprc* zebrafish, *Tg(fabp10:Cre)/lrpprc*$^{GBT0235/GBT0235}$ line that could then be scored
582 for loss of liver-specific mRFP (Supplementary Figure 2) and tested for reversion of the
583 homozygous mutant phenotypes. Following the generation of this line, we replicated the survival
584 experiments to assess the lipid metabolism to determine whether we would see an improvement
585 in liver function. Overall, we noted a decrease in the cholesterol and neutral lipid accumulation
586 in the Oil Red O staining in the liver rescue conditions (Figure 6F and 6G). We also saw a
587 reversion of the lethality in larvae with a mutant allele with 85% of those with the liver rescue
588 surviving until at least 12 dpf (Figure 6H). Liver-specific rescue in the homozygous mutant
589 background reverted the mitochondrial morphology restoring the regular cristae network in
590 hepatocytes (Figure 6K and 6L).

591 **The altered dietary lipid metabolism in *lrpprc*$^{GBT0235/GBT0235}$ mutants is restored to wildtype**
592 **levels through liver-specific rescue methods**

593 To test the hypothesis that healthy liver function may exert a protective role to overall health in
594 the context of mitochondrial disease, we rescued the liver phenotype of *lrpprc* homozygous
595 mutants by crossing them with a liver-specific Cre recombinase transgenic line and performing
596 an in cross of the double transgenic animals. Since we found altered lipid metabolism in the
597 *lrpprc* null mutants using HPLC methods, we asked whether the liver-specific rescue restores

598 metabolic function to wildtype levels. Not only did the liver-specific rescued null mutants ingest
599 as much as their wildtype and heterozygous siblings, as measured by their non-metabolizable
600 TopFluor Cholesterol peak area, the total peak area of nonpolar lipids were lowered to that of the
601 wildtype siblings (*lrpprc*$^{GBT0235/GBT0235}$; *Tg(fabp10:Cre)/lrpprc*$^{GBT0235/GBT0235}$ = 0.542; 95% CI =
602 0.357–0.823, p = 0.004; (Figure 7A)). The genetic background of the liver-specific CRE rescue
603 did not contribute to any change in lipid levels (*Tg(fab10:Cre)lrpprc*$^{+/+}$*:lrpprc*$^{+/+}$] = 0.944; 95%
604 CI = 0.640–1.391, z = -0.2934, p = 0.769; (Figure 7D)).

605 **Discussion**

606 In this study, we present a novel zebrafish model for Leigh Syndrome, French Canadian Type
607 (LSFC) identified through the RP2 gene-breaking transposon insertional mutagenesis screen.
608 Phenotypic assessment of this novel allele demonstrates how zebrafish serve as an excellent
609 model to study LSFC. Lrpprc, shares 51% homology and conserved PPR domains with its
610 human ortholog. Bioinformatic analysis starting with the human PPR domains with BLASTP
611 revealed 16 predicted similar PPR domains in the zebrafish *lrpprc* gene indicating the conserved
612 mitochondrial mRNA binding role of this gene in this vertebrate (Supplementary Figure 3). On
613 the basis of location of the RP2 insertion, the RFP protein is predicted to fuse with the N-
614 terminal 793 amino acids of Lrpprc. The spatiotemporal analysis of Lrpprc-mRFP shows a co-
615 localization with an established mitochondrial marker in the caudal fin region and myocytes, as
616 the truncated fusion proteins retains the predicted mitochondrial targeting sequence (1-77 amino
617 acids), maintaining its predicted sub-cellular localization. We also observed remarkable
618 ubiquitous expression patterns throughout the organism and hotspots in the liver, skeletal muscle,
619 and eye (Figure 1B). In addition, increased expression of the fusion protein in certain tissues
620 such as the liver, skeletal muscle, and eyes is indicative of the observation that mitochondrial
621 density is tied to energy intensive processes like metabolism, movement, and vision. Different
622 expression data will nevertheless help in expanding our understanding of different roles of this
623 gene in tissue-specific niches.

624 As the pathophysiology of LSFC is not well understood, we set out to explore the physiological
625 consequences of a *lrpprc* loss-of-function mutation *in vivo* and whether we could mimic the
626 clinical hallmarks seen in LSFC patients. Mutations in *LRPPRC* are associated with infant
627 mortality marked by episodes of fatal acidotic crisis contributing to infant mortality (Morin et al.,

628 1993). Similarly, homozygous *lrpprc* mutant zebrafish displayed complete larval lethality by 12
629 dpf. However, factors triggering the crisis and associated death in both patients and animal
630 model was initially unclear. Decreased steady state levels of mitochondrially encoded transcripts
631 is another hallmark that is presented in patients with LRPPRC deficiency. Previous studies have
632 implicated LRPPRC to be a critical post-transcriptional regulator of mitochondrial transcripts.
633 LRPPRC regulates the process by the formation of a complex with SRA Stem-Loop Interacting
634 RNA Binding Protein (SLIRP) that recruits mitochondrial polyA polymerase (MTPAP) to
635 initiate the polyadenylation of these transcripts (Ruzzenente et al., 2012). It also acts as a global
636 RNA chaperone stabilizing the mRNA structure and inhibits the 3' exonucleolytic mRNA
637 degradation regulated by Polynucleotide Phosphorylase (PNPase) and Suppressor of Var1, 3
638 (SUV3) (Chujo et al., 2012; Siira et al., 2017). Consistent with the previous *in vitro* studies
639 (Gohil et al., 2010), expression of mitochondrial protein coding transcripts was observed to be
640 downregulated in these homozygous mutants by more than 2-fold and were further investigated
641 using RNASeq.

642 Decreased expression of these protein-coding transcripts is crucial for eliciting defects in the
643 oxidative phosphorylation and mitochondrial respiratory chain. These results were in
644 concordance with the pathways responsible for mitochondrial biogenesis and homeostasis
645 predicted to be depleted in the *lrpprc* homozygous mutants. In addition to the depleted
646 respiratory electron transport and complex 1 biogenesis, bioinformatic analyses also revealed
647 depleted pyruvate metabolism, mitochondrial translation termination and hepatic mitochondrial
648 resident pathway such as metabolism of xenobiotics by cytochrome P450. Various functions
649 including energy production, genome maintenance, ion/metabolite homeostasis, membrane
650 dynamics and transport of biomolecules can be attributed to approximately 1158 nuclear proteins
651 residing in mitochondria (Calvo et al., 2016). We did note an overlap between the set of
652 differentially expressed genes and these 1158 MitoCarta genes, suggesting an altered
653 mitochondrial transcriptome signature. Apart from classical respiratory chain subunits, we
654 identified some key genes from this overlapped data to be differentially expressed that were
655 responsible in pathways such as aldehyde metabolism, fatty acid metabolism and most important,
656 unfolded protein response. Pyruvate dehydrogenase kinase 2b (*pdk2b*) was downregulated in
657 the null mutants and is known to play an important role in the metabolism of fatty acids by
658 inhibiting the pyruvate dehydrogenase activity which inhibits the formation of acetyl-coenzyme

659 A. The expression of mitochondrial isoform of aldehyde dehydrogenase 2 family member,
660 tandem duplicate 2 (*aldh2.2*) was also downregulated, possibly suggesting an interconnection
661 between aldehyde metabolism and detoxification of lipid peroxidation by-products in
662 mitochondria (Nene et al., 2017). *lrpprc* homozygous mutants exhibited an upregulation of
663 chaperones proteins, heat shock protein 60 (*hsp60*) and heat shock protein (*hsp70*) that form an
664 integral part of mitochondrial unfolded protein response. Knockdown of *lrpprc* in a mammalian
665 cell model has been shown to elicit mitochondrial unfolded protein response triggered by nuclear
666 encoded and mitochondrial encoded subunits of complex IV of mitochondrial electron transport
667 chain (Kohler et al., 2015).

668 Another high energy-requisition tissue on the phenotypic spectrum of LSFC that we explored
669 was muscle. LSFC patients display muscle defects such as hypotonia and COX deficiency
670 (Olahova et al., 2015) and therefore, we adopted a birefringence measurement (Smith et al.,
671 2013) to assess the muscle phenotype in our null mutants. It takes a complex and highly
672 organized structure (like the sarcomeres in skeletal muscle) to rotate the plane polarized light and
673 enable the visualization of birefringence. The noted decrease in birefringence in *lrpprc* mutants
674 is most likely due to the disorganization of sarcomeres and other structures in skeletal muscle.
675 The findings here did concur with those from the transcriptomic studies where key muscle
676 related genes such as myogenic differentiation 1 (*myod1*) and dysferlin (*dysf*) were observed to
677 be differentially expressed. We found *myod1*, a gene involved in muscle regeneration to be
678 downregulated in our study. *dysf* was upregulated in *lrprrc* homozygous mutant larvae, and *Dysf*
679 overexpression was noted in mice to cause muscle defects, including kyphosis and irregular gait
680 (Glover et al., 2010). In addition, we observed the pathway for striated muscle contraction to also
681 show reduced expression in *lrpprc* mutant larvae. Cysteine rich protein 1 b (*csrp1b*), the gene
682 responsible for smooth muscle differentiation and muscle development (Henderson et al., 1999),
683 was also found to be expressed in low levels in the *lrpprc* homozygous mutants.

684 The liver-specific dysfunction coupled with the episodes of acute metabolic crises distinguishes
685 LSFC from classic Leigh Syndrome (LS). A previous study suggested that liver dysfunction may
686 factor into the increased lactic acidosis and metabolic disturbances as the liver plays a key role in
687 lactate homeostasis via the Cori cycle (Sun et al., 2017). In addition, it is important to note that
688 other basic liver functions that are dependent on mitochondrial activity such as lipid metabolism,
689 serum detoxification, and gluconeogenesis may be key to the development of metabolic crises

690 since they have secondary effects in other organ systems. Under TEM, mitochondrial
691 morphology was altered in the mutants with reduced or collapsed cristae in the hepatocytes,
692 possibly suggesting an impaired mitochondrial function. It has been observed that mitochondrial
693 disorders increase predisposition to intracellular lipid accumulation (Morino et al., 2006).
694 Homozygous *lrpprc* mutants manifested early onset phenotypes with hepatomegaly and
695 progressive accumulation of dark-colored granules in the liver at 6 dpf. These granules appeared
696 to be lipid droplets, which was validated with both Oil Red O staining and extensive *in vivo*
697 feed/chase (i.e., metabolize) labeling lipid studies.

698 Dietary lipid metabolism studies in the homozygous mutants revealed accumulation of non-polar
699 lipids such as triacylglycerides and diacylglycerides. Accumulation of these lipid species
700 highlights an impaired lipid metabolism in the mutants similar to what is observed in LSFC
701 patients (Ruiz et al., 2019). Metabolic diseases such as nonalcoholic fatty liver disease are
702 associated with accumulation of triglyceride levels and high low-density lipoprotein levels with
703 an underlying mitochondrial dysfunction (Simoes et al., 2018). Hepatic accumulation of such
704 lipids may induce mitochondria to undergo dynamic changes such as depolarization and loss of
705 ATP content (Dominguez-Perez et al., 2019). Further probing of the transcriptomics study
706 revealed that pathways pertaining to fatty acid degradation were depleted in these null mutants.
707 The gene encoding for acyl-coA dehydrogenase medium chain (*Acadm*), a protein that plays an
708 important role in the fatty acid oxidation by making medium-chain acyl-CoA dehydrogenase
709 enzyme was downregulated approximately by fold change of $\log_2$ 1.5. Catalysis of desaturation
710 of acyl-CoAs to 2-trans-enoyl-CoAs, first step in the fatty acid beta-oxidation pathway, is
711 regulated by acyl-CoA oxidase 1, palmitoyl (*acox1*), expression of which was reduced in mutant
712 larvae. Fatty acid beta-oxidation is not only an exclusive mitochondrial resident pathway but also
713 occurs in peroxisomes. Intrigued to explore that, if the abolishment of *lrpprc* had an inter-
714 organelle effect, we analysed the expression of genes that are involved in peroxisome associated
715 pathways. Surprisingly, MPV17 mitochondrial inner membrane protein like 2 (*mpv17l2*), one of
716 the regulator genes for expression of antioxidant enzymes, was upregulated by fold change of
717 $\log_2$ 2. Previous study has described that its human ortholog *MPV17L2* downregulates the
718 expression of glutathione peroxidase and catalase genes (Iida et al., 2006). This mechanism was
719 replicated in our mutants where we observed the expression of these genes to be decreased by a
720 fold change of $\log_2$ 1.7 and $\log_2$ 1.9 respectively. Overall, our zebrafish LSFC model exhibited a

721 dysfunctional mitochondrial signature both at the transcriptional and phenotypic level, utility of
722 which was explored to design a genetic model therapy for LSFC associated phenotypes.

723 Because GBT-RP2 contains two loxP sites flanking the protein trap component, we could exploit
724 this utility to rescue the organ specific function of *lrpprc*$^{GBT0235/GBT0235}$. To test the hypothesis
725 that liver function might exert a protective role in mitochondrial disease, we induced liver-
726 specific expression of *lrpprc*$^{GBT0235/GBT0235}$ by removal of the GBT cassette via liver-specific Cre
727 recombinase. Interestingly, mRFP expression was exclusively extinguished in the liver and
728 reversion of both survival and biochemical phenotypes was observed, suggesting the liver plays a
729 critical role in the pathology of LSFC. Remarkably, these liver-specific rescued larvae exhibited
730 similar levels of non-polar lipids as compared to the wild type larvae, post high-fat meal
731 underscoring the lipid homeostasis as a key therapeutic paradigm in the progression of this
732 disease. Mitigation of abnormal mitochondrial structure with collapsed cristae was also observed
733 in the hepatocytes of the rescued larvae. This effect may in part be due to the restoration of
734 levels of mitochondrial transcripts and thus restoring mitochondrial mediated liver functions
735 such as beta oxidation, fatty acid elongation, cycling of cytochrome molecules and
736 gluconeogenesis. We anticipate that these results, together with those from the conditional
737 knockout experiments will enhance our understanding of the function of *lrpprc* gene in hepatic
738 lipid homeostasis and perhaps shine a light towards new therapeutic options.

739 With advances in gene editing alongside developments in both viral and non-viral vector
740 delivery, there is hope for tissue-specific gene therapy as a potential avenue to help
741 mitochondrial disease patients. Our findings raise the question whether advances in gene therapy
742 could be used as a therapeutic for patients of LSFC by rescuing *lrpprc* expression in the liver.
743 Since stability of the mitochondrial mRNA transcript, but not its sequence, is disturbed in LSFC,
744 we postulate that inhibiting the mitochondrial RNA degradation pathway may also be a novel
745 therapeutic avenue. Zebrafish are amenable for large-scale drug screens and are increasingly
746 being used for this purpose due to the ease of administration of pharmaceutical compounds.
747 Remarkably, the *lrprrc* homozygous mutants developed various hallmarks of LSFC including
748 decreased mitochondrial transcript stability, aberrant mitochondrial morphology, hepatic
749 steatosis, increased triglyceride levels and early death. Reversion of these measures back to wild
750 type levels could be used as a readout of therapeutic drug candidates.

751 **Acknowledgements**

752 The authors thank Ms. Mrunal Dehankar of the Mayo Clinic Bioinformatics core for the primary
753 bioinformatics analyses. The authors also thank the Mayo Clinic Zebrafish Facility staff who
754 contributed to the generation of the zebrafish line and the Mayo Clinic Microscopy Cell Analysis
755 and Core for imaging facility. We would also like to acknowledge Mike Sepanski and Vanessa
756 Quinlivan of the Carnegie Institution for the TEM imaging and assistance with HPLC,
757 respectively. This work was funded by NIH grants GM63904 and DA14546, the Marriott
758 Foundation, the Mayo Foundation, R01 DK093399 (Farber, PI). Additional support for this work
759 was provided by the Carnegie Institution for Science Endowment and the G. Harold and Leila Y.
760 Mathers Charitable Foundation. *Tg(−2.8fabp10:Cre; −0.8cryaa:Venus)*^{S955} zebrafish transgenic
761 line was a kind gift from Dr. W. Chen, Vanderbilt University, Nashville, TN, USA.
762 *Tg(MLS:EGFP)* zebrafish transgenic line was a kind gift from Dr. S. Sivasubbu, CSIR-IGIB,
763 India and Dr. S. Choi, Chonnam Medical School, South Korea.

764 **Author Contributions**

765 The paper was written by AS, MDW, JLA and SCE. Experiments were executed by AS, MDW,
766 RLC, MRS, JLA, AJT, NI, WL, JY, YDing, YDeng with experimental guidance from XX, KJC,
767 SAF and SCE. Data analysis was completed by AS, MDW, RLC, JLA, MRS, AJT, NI, WL.
768

769 ## References

770 Bolger AM, Lohse M, Usadel B. 2014. Trimmomatic: a flexible trimmer for Illumina sequence
771 data. *Bioinformatics* **30**:2114–2120. doi:10.1093/bioinformatics/btu170

772 Bray NL, Pimentel H, Melsted P, Pachter L. 2016. Near-optimal probabilistic RNA-seq
773 quantification. *Nat Biotechnol* **34**:525–527. doi:10.1038/nbt.3519

774 Broughton RE, Milam JE, Roe BA. 2001. The complete sequence of the zebrafish (Danio rerio)
775 mitochondrial genome and evolutionary patterns in vertebrate mitochondrial DNA. *Genome*
776 *Res*. doi:10.1101/gr.156801

777 Byrnes J, Ganetzky R, Lightfoot R, Tzeng M, Nakamaru-Ogiso E, Seiler C, Falk MJ. 2018.
778 Pharmacologic modeling of primary mitochondrial respiratory chain dysfunction in
779 zebrafish. *Neurochem Int*. doi:10.1016/j.neuint.2017.07.008

780 Calvo SE, Clauser KR, Mootha VK. 2016. MitoCarta2.0: an updated inventory of mammalian
781 mitochondrial proteins. *Nucleic Acids Res* **44**:D1251-7. doi:10.1093/nar/gkv1003

782 Carten JD, Bradford MK, Farber SA. 2011. Visualizing digestive organ morphology and
783 function using differential fatty acid metabolism in live zebrafish. *Dev Biol*.
784 doi:10.1016/j.ydbio.2011.09.010

785 Chinnery PF, Elliott HR, Hudson G, Samuels DC, Relton CL. 2012. Epigenetics, epidemiology
786 and mitochondrial DNA diseases. *Int J Epidemiol* **41**:177–187. doi:10.1093/ije/dyr232

787 Chujo T, Ohira T, Sakaguchi Y, Goshima N, Nomura N, Nagao A, Suzuki T. 2012.
788 LRPPRC/SLIRP suppresses PNPase-mediated mRNA decay and promotes polyadenylation
789 in human mitochondria. *Nucleic Acids Res* **40**:8033–8047. doi:10.1093/nar/gks506

790 Clark KJ, Balciunas D, Pogoda H-M, Ding Y, Westcot SE, Bedell VM, Greenwood TM, Urban
791 MD, Skuster KJ, Petzold AM, Ni J, Nielsen AL, Patowary A, Scaria V, Sivasubbu S, Xu X,
792 Hammerschmidt M, Ekker SC. 2011. In vivo protein trapping produces a functional
793 expression codex of the vertebrate proteome. *Nat Methods* **8**:506–515.
794 doi:10.1038/nmeth.1606

795 Cui J, Wang L, Ren X, Zhang Y, Zhang H. 2019. LRPPRC: A Multifunctional Protein Involved
796 in Energy Metabolism and Human Disease. *Front Physiol*. doi:10.3389/fphys.2019.00595

797 Cuillerier A, Honarmand S, Cadete VJJ, Ruiz M, Forest A, Deschenes S, Beauchamp C, Charron
798 G, Rioux JD, Des Rosiers C, Shoubridge EA, Burelle Y. 2017. Loss of hepatic LRPPRC
799 alters mitochondrial bioenergetics, regulation of permeability transition and trans-
800 membrane ROS diffusion. *Hum Mol Genet* **26**:3186–3201. doi:10.1093/hmg/ddx202

801 Debray F-G, Morin C, Janvier A, Villeneuve J, Maranda B, Laframboise R, Lacroix J, Decarie J-
802 C, Robitaille Y, Lambert M, Robinson BH, Mitchell GA. 2011. LRPPRC mutations cause a
803 phenotypically distinct form of Leigh syndrome with cytochrome c oxidase deficiency. *J*

Med Genet **48**:183–189. doi:10.1136/jmg.2010.081976

Dominguez-Perez M, Simoni-Nieves A, Rosales P, Nuno-Lambarri N, Rosas-Lemus M, Souza V, Miranda RU, Bucio L, Uribe Carvajal S, Marquardt JU, Seo D, Gomez-Quiroz LE, Gutierrez-Ruiz MC. 2019. Cholesterol burden in the liver induces mitochondrial dynamic changes and resistance to apoptosis. *J Cell Physiol* **234**:7213–7223. doi:10.1002/jcp.27474

Flinn L, Mortiboys H, Volkmann K, Kster RW, Ingham PW, Bandmann O. 2009. Complex i deficiency and dopaminergic neuronal cell loss in parkin-deficient zebrafish (Danio rerio). *Brain*. doi:10.1093/brain/awp108

Glover LE, Newton K, Krishnan G, Bronson R, Boyle A, Krivickas LS, Brown RHJ. 2010. Dysferlin overexpression in skeletal muscle produces a progressive myopathy. *Ann Neurol* **67**:384–393. doi:10.1002/ana.21926

Gohil VM, Nilsson R, Belcher-Timme CA, Luo B, Root DE, Mootha VK. 2010. Mitochondrial and nuclear genomic responses to loss of LRPPRC expression. *J Biol Chem* **285**:13742–13747. doi:10.1074/jbc.M109.098400

Gorman GS, Chinnery PF, DiMauro S, Hirano M, Koga Y, McFarland R, Suomalainen A, Thorburn DR, Zeviani M, Turnbull DM. 2016. Mitochondrial diseases. *Nat Rev Dis Prim* **2**:16080. doi:10.1038/nrdp.2016.80

Green DR. 1998. Apoptotic pathways: the roads to ruin. *Cell* **94**:695–698. doi:10.1016/s0092-8674(00)81728-6

Henderson JR, Macalma T, Brown D, Richardson JA, Olson EN, Beckerle MC. 1999. The LIM protein, CRP1, is a smooth muscle marker. *Dev Dyn* **214**:229–238. doi:10.1002/(SICI)1097-0177(199903)214:3<229::AID-AJA6>3.0.CO;2-S

Ichino N, Serres M, Urban R, Urban M, Schaefbauer K, Greif L, Varshney GK, Skuster KJ, McNulty M, Daby C, Wang Y, Liao H, El-Rass S, Ding Y, Liu W, Schimmenti LA, Sivasubbu S, Balciunas D, Hammerschmidt M, Farber SA, Wen X-Y, Xu X, McGrail M, Essner JJ, Burgess S, Clark KJ, Ekker SC. 2019. The Vertebrate Codex Gene Breaking Protein Trap Library For Genomic Discovery and Disease Modeling Applications. *bioRxiv* 630236. doi:10.1101/630236

Iida R, Yasuda T, Tsubota E, Takatsuka H, Matsuki T, Kishi K. 2006. Human Mpv17-like protein is localized in peroxisomes and regulates expression of antioxidant enzymes. *Biochem Biophys Res Commun* **344**:948–954. doi:10.1016/j.bbrc.2006.04.008

Kim MJ, Kang KH, Kim CH, Choi SY. 2008. Real-time imaging of mitochondria in transgenic zebrafish expressing mitochondrially targeted GFP. *Biotechniques*. doi:10.2144/000112909

Kim S-H, Scott SA, Bennett MJ, Carson RP, Fessel J, Brown HA, Ess KC. 2013. Multi-organ abnormalities and mTORC1 activation in zebrafish model of multiple acyl-CoA dehydrogenase deficiency. *PLoS Genet* **9**:e1003563. doi:10.1371/journal.pgen.1003563

840 Kohler F, Muller-Rischart AK, Conradt B, Rolland SG. 2015. The loss of LRPPRC function
841 induces the mitochondrial unfolded protein response. *Aging (Albany NY)* **7**:701–717.
842 doi:10.18632/aging.100812

843 Lambert CJ, Freshner BC, Chung A, Stevenson TJ, Bowles DM, Samuel R, Gale BK,
844 Bonkowsky JL. 2018. An automated system for rapid cellular extraction from live zebrafish
845 embryos and larvae: Development and application to genotyping. *PLoS One* **13**:e0193180.
846 doi:10.1371/journal.pone.0193180

847 Lieschke GJ, Currie PD. 2007. Animal models of human disease: Zebrafish swim into view. *Nat*
848 *Rev Genet*. doi:10.1038/nrg2091

849 Liu L, McKeehan WL. 2002. Sequence analysis of LRPPRC and its SEC1 domain interaction
850 partners suggests roles in cytoskeletal organization, vesicular trafficking, nucleocytosolic
851 shuttling, and chromosome activity. *Genomics*. doi:10.1006/geno.2001.6679

852 Love MI, Huber W, Anders S. 2014. Moderated estimation of fold change and dispersion for
853 RNA-seq data with DESeq2. *Genome Biol* **15**:550. doi:10.1186/s13059-014-0550-8

854 Manna S. 2015. An overview of pentatricopeptide repeat proteins and their applications.
855 *Biochimie*. doi:10.1016/j.biochi.2015.04.004

856 McFarland R, Taylor RW, Turnbull DM. 2010. A neurological perspective on mitochondrial
857 disease. *Lancet Neurol* **9**:829–840. doi:10.1016/S1474-4422(10)70116-2

858 Mi H, Muruganujan A, Huang X, Ebert D, Mills C, Guo X, Thomas PD. 2019. Protocol Update
859 for large-scale genome and gene function analysis with the PANTHER classification system
860 (v.14.0). *Nat Protoc* **14**:703–721. doi:10.1038/s41596-019-0128-8

861 Mili S, Piñol-Roma S. 2003. LRP130, a Pentatricopeptide Motif Protein with a Noncanonical
862 RNA-Binding Domain, Is Bound In Vivo to Mitochondrial and Nuclear RNAs. *Mol Cell*
863 *Biol*. doi:10.1128/mcb.23.14.4972-4982.2003

864 Mootha VK, Lepage P, Miller K, Bunkenborg J, Reich M, Hjerrild M, Delmonte T, Villeneuve
865 A, Sladek R, Xu F, Mitchell GA, Morin C, Mann M, Hudson TJ, Robinson B, Rioux JD,
866 Lander ES. 2003. Identification of a gene causing human cytochrome c oxidase deficiency
867 by integrative genomics. *Proc Natl Acad Sci U S A* **100**:605–610.
868 doi:10.1073/pnas.242716699

869 Moraes CT, Ricci E, Bonilla E, DiMauro S, Schon EA. 1992. The mitochondrial
870 tRNA(Leu(UUR)) mutation in mitochondrial encephalomyopathy, lactic acidosis, and
871 strokelike episodes (MELAS): genetic, biochemical, and morphological correlations in
872 skeletal muscle. *Am J Hum Genet* **50**:934–949.

873 Morin C, Mitchell G, Larochelle J, Lambert M, Ogier H, Robinson BH, De Braekeleer M. 1993.
874 Clinical, metabolic, and genetic aspects of cytochrome C oxidase deficiency in Saguenay-
875 Lac-Saint-Jean. *Am J Hum Genet* **53**:488–496.

876 Morino K, Petersen KF, Shulman GI. 2006. Molecular mechanisms of insulin resistance in
877 humans and their potential links with mitochondrial dysfunction. *Diabetes* **55 Suppl 2**:S9–
878 S15. doi:10.2337/db06-S002

879 Nene A, Chen C-H, Disatnik M-H, Cruz L, Mochly-Rosen D. 2017. Aldehyde dehydrogenase 2
880 activation and coevolution of its epsilonPKC-mediated phosphorylation sites. *J Biomed Sci*
881 **24**:3. doi:10.1186/s12929-016-0312-x

882 Newsholme P, Gaudel C, Krause M. 2012. Mitochondria and diabetes. An intriguing
883 pathogenetic role. *Adv Exp Med Biol* **942**:235–247. doi:10.1007/978-94-007-2869-1_10

884 Olahova M, Hardy SA, Hall J, Yarham JW, Haack TB, Wilson WC, Alston CL, He L,
885 Aznauryan E, Brown RM, Brown GK, Morris AAM, Mundy H, Broomfield A, Barbosa IA,
886 Simpson MA, Deshpande C, Moeslinger D, Koch J, Stettner GM, Bonnen PE, Prokisch H,
887 Lightowlers RN, McFarland R, Chrzanowska-Lightowlers ZMA, Taylor RW. 2015.
888 LRPPRC mutations cause early-onset multisystem mitochondrial disease outside of the
889 French-Canadian population. *Brain* **138**:3503–3519. doi:10.1093/brain/awv291

890 Plucińska G, Paquet D, Hruscha A, Godinho L, Haass C, Schmid B, Misgeld T. 2012. In vivo
891 imaging of disease-related mitochondrial dynamics in a vertebrate model system. *J*
892 *Neurosci*. doi:10.1523/JNEUROSCI.1327-12.2012

893 Quinlivan VH, Wilson MH, Ruzicka J, Farber SA. 2017. An HPLC-CAD/fluorescence
894 lipidomics platform using fluorescent fatty acids as metabolic tracers. *J Lipid Res* **58**:1008–
895 1020. doi:10.1194/jlr.D072918

896 Rahman S, Blok RB, Dahl HH, Danks DM, Kirby DM, Chow CW, Christodoulou J, Thorburn
897 DR. 1996. Leigh syndrome: clinical features and biochemical and DNA abnormalities. *Ann*
898 *Neurol* **39**:343–351. doi:10.1002/ana.410390311

899 Rizzuto R, Marchi S, Bonora M, Aguiari P, Bononi A, De Stefani D, Giorgi C, Leo S, Rimessi
900 A, Siviero R, Zecchini E, Pinton P. 2009. Ca(2+) transfer from the ER to mitochondria:
901 when, how and why. *Biochim Biophys Acta* **1787**:1342–1351.
902 doi:10.1016/j.bbabio.2009.03.015

903 Ruiz M, Cuillerier A, Daneault C, Deschenes S, Frayne IR, Bouchard B, Forest A, Legault JT,
904 Vaz FM, Rioux JD, Burelle Y, Des Rosiers C. 2019. Lipidomics unveils lipid
905 dyshomeostasis and low circulating plasmalogens as biomarkers in a monogenic
906 mitochondrial disorder. *JCI insight* **4**. doi:10.1172/jci.insight.123231

907 Ruzzenente B, Metodiev MD, Wredenberg A, Bratic A, Park CB, Camara Y, Milenkovic D,
908 Zickermann V, Wibom R, Hultenby K, Erdjument-Bromage H, Tempst P, Brandt U,
909 Stewart JB, Gustafsson CM, Larsson N-G. 2012. LRPPRC is necessary for polyadenylation
910 and coordination of translation of mitochondrial mRNAs. *EMBO J* **31**:443–456.
911 doi:10.1038/emboj.2011.392

912 Sabharwal A, Campbell JM, WareJoncas Z, Wishman M, Ata H, Liu W, Ichino N, Bergren JD,

913 Urban MD, Urban R, Poshusta TL, Ding Y, Xu X, Clark KJ, Ekker SC. 2019a. A primer
914 genetic toolkit for exploring mitochondrial biology and disease using zebrafish. *bioRxiv*.
915 doi:10.1101/542084

916 Sabharwal A, Sharma D, Vellarikkal SK, Jayarajan R, Verma A, Senthivel V, Scaria V,
917 Sivasubbu S. 2019b. Organellar transcriptome sequencing reveals mitochondrial
918 localization of nuclear encoded transcripts. *Mitochondrion* **46**:59–68.
919 doi:10.1016/j.mito.2018.02.007

920 Sasarman F, Nishimura T, Antonicka H, Weraarpachai W, Shoubridge EA. 2015. Tissue-specific
921 responses to the LRPPRC founder mutation in French Canadian Leigh Syndrome. *Hum Mol*
922 *Genet* **24**:480–491. doi:10.1093/hmg/ddu468

923 Siira SJ, Spahr H, Shearwood A-MJ, Ruzzenente B, Larsson N-G, Rackham O, Filipovska A.
924 2017. LRPPRC-mediated folding of the mitochondrial transcriptome. *Nat Commun* **8**:1532.
925 doi:10.1038/s41467-017-01221-z

926 Simoes ICM, Fontes A, Pinton P, Zischka H, Wieckowski MR. 2018. Mitochondria in non-
927 alcoholic fatty liver disease. *Int J Biochem Cell Biol* **95**:93–99.
928 doi:10.1016/j.biocel.2017.12.019

929 Smith LL, Beggs AH, Gupta VA. 2013. Analysis of skeletal muscle defects in larval zebrafish by
930 birefringence and touch-evoke escape response assays. *J Vis Exp*. doi:10.3791/50925

931 Soneson C, Love MI, Robinson MD. 2015. Differential analyses for RNA-seq: transcript-level
932 estimates improve gene-level inferences. *F1000Research* **4**:1521.
933 doi:10.12688/f1000research.7563.2

934 Song Y, Selak MA, Watson CT, Coutts C, Scherer PC, Panzer JA, Gibbs S, Scott MO, Willer G,
935 Gregg RG, Ali DW, Bennett MJ, Balice-Gordon RJ. 2009. Mechanisms underlying
936 metabolic and neural defects in zebrafish and human multiple Acyl-CoA dehydrogenase
937 deficiency (MADD). *PLoS One*. doi:10.1371/journal.pone.0008329

938 Spinelli JB, Haigis MC. 2018. The multifaceted contributions of mitochondria to cellular
939 metabolism. *Nat Cell Biol* **20**:745–754. doi:10.1038/s41556-018-0124-1

940 Steele SL, Prykhozhij S V., Berman JN. 2014. Zebrafish as a model system for mitochondrial
941 biology and diseases. *Transl Res*. doi:10.1016/j.trsl.2013.08.008

942 Sterky FH, Ruzzenente B, Gustafsson CM, Samuelsson T, Larsson N-G. 2010. LRPPRC is a
943 mitochondrial matrix protein that is conserved in metazoans. *Biochem Biophys Res*
944 *Commun* **398**:759–764. doi:10.1016/j.bbrc.2010.07.019

945 Stockel D, Kehl T, Trampert P, Schneider L, Backes C, Ludwig N, Gerasch A, Kaufmann M,
946 Gessler M, Graf N, Meese E, Keller A, Lenhof H-P. 2016. Multi-omics enrichment analysis
947 using the GeneTrail2 web service. *Bioinformatics* **32**:1502–1508.
948 doi:10.1093/bioinformatics/btv770

949 Sun S, Li H, Chen J, Qian Q. 2017. Lactic Acid: No Longer an Inert and End-Product of
950 Glycolysis. *Physiology (Bethesda)* **32**:453–463. doi:10.1152/physiol.00016.2017

951 Tiku V, Tan M-W, Dikic I. 2020. Mitochondrial Functions in Infection and Immunity. *Trends*
952 *Cell Biol* **30**:263–275. doi:10.1016/j.tcb.2020.01.006

953 Urrutia PJ, Mena NP, Nunez MT. 2014. The interplay between iron accumulation, mitochondrial
954 dysfunction, and inflammation during the execution step of neurodegenerative disorders.
955 *Front Pharmacol* **5**:38. doi:10.3389/fphar.2014.00038

956 Vafai SB, Mootha VK. 2012. Mitochondrial disorders as windows into an ancient organelle.
957 *Nature* **491**:374–383. doi:10.1038/nature11707

958 Valero T. 2014. Mitochondrial biogenesis: pharmacological approaches. *Curr Pharm Des*.
959 doi:10.2174/1381612820351409111421 18

960 Wallace DC. 2012. Mitochondria and cancer. *Nat Rev Cancer* **12**:685–698. doi:10.1038/nrc3365

961 Wilkinson RN, Elworthy S, Ingham PW, van Eeden FJM. 2017. Fin clipping and genotyping
962 embryonic zebrafish at 3 days post-fertilization. *Biotechniques*. doi:10.2144/000114509

963 Wilson MH, Rajan S, Danoff A, White RJ, Hensley MR, Quinlivan VH, Thierer JH, Busch-
964 Nentwich EM, Hussain MM, Farber SA. 2019. A missense mutation dissociates triglyceride
965 and phospholipid transfer activities in zebrafish and human microsomal triglyceride transfer
966 protein. *bioRxiv* 701813. doi:10.1101/701813

967 Xu F, Addis JBL, Cameron JM, Robinson BH. 2012. LRPPRC mutation suppresses cytochrome
968 oxidase activity by altering mitochondrial RNA transcript stability in a mouse model.
969 *Biochem J* **441**:275–283. doi:10.1042/BJ20110985

970 Zeituni EM, Wilson MH, Zheng X, Iglesias PA, Sepanski MA, Siddiqi MA, Anderson JL, Zheng
971 Y, Farber SA. 2016. Endoplasmic reticulum lipid flux influences enterocyte nuclear
972 morphology and lipid-dependent transcriptional responses. *J Biol Chem*.
973 doi:10.1074/jbc.M116.749358

974

975 ## Figures Legends

976 **Figure 1: GBT mutagenesis generates a novel zebrafish model of LSFC. (A)** Schematic of
977 human and zebrafish LRPPRC proteins with highlighted PPR domains (denoted by P). **(B)**
978 Schematic of the integration event of GBT vector RP2.1 with 5' protein trap and 3' exon trap
979 cassettes. The RP2.1 cassette was integrated in the intronic region 22 of the lrpprc genomic locus
980 on chromosome 13. ITR, inverted terminal repeat; SA, loxP; Cre recombinase recognition
981 sequence, splice acceptor; *mRFP' AUG-less mRFP sequence; poly (A)+, polyadenylation
982 signal; red octagon, extra transcriptional terminator and putative border element; β-act, carp beta-
983 actin enhancer, SD, splice donor

984 **Figure 2: Spatiotemporal expression of Lrpprc-mRFP in GBT0235 mutants. (A)**
985 Representative images of 6dpf *lrpprc* heterozygous mutants (*lrpprc*$^{GBT0235/+}$) with bright RFP
986 expression in the liver and gut (magnification-5X; Scale bar: 200 µm). **(B)** Relative expression of
987 *lrpprc* transcript in wild type (denoted by '++"; *lrpprc*$^{+/+}$) and homozygous mutant larvae
988 (denoted by "-/-"; *lrpprc*$^{GBT0235/GBT0235}$) (p-value <0.001). **(C)** 2 dpf *Tg(MLS:EGFP)*
989 *lrprrc*$^{GBT0235/+}$ was used to observe the sub-cellular localization of the *lrpprc* protein in the caudal
990 fin region. Mitochondria were detected with fluoescence microscopy under GFP filter while the
991 truncated lrprrc:mRFP fusion protein was detected using an RFP filter.

992 **Figure 3: *lrpprc* homozygous zebrafish mutants recapitulate the hallmarks of Leigh**
993 **syndrome French-Canadian type**. **(A)** Survival percentage of three genotypes, wild type
994 *lrpprc*$^{+/+}$, heterozygous- *lrpprc*$^{GBT0235/+}$ and homozygous mutants- *lrpprc*$^{GBT0235/GBT0235}$. Data is
995 represented from independent experiments (p-value <0.05). **(B)** Relative expression of
996 mitochondrial encoded transcripts in the homozygous and wild type siblings assessed by qRT-
997 PCR. Nuclear encoded genes, *rps6kb1 and nfe2l2a* were used as control. Black circle represent
998 wild type and red triangle represent homozygous mutants. Mitochondrial transcripts were
999 normalized to *eef1a1l1* transcript levels. Error bars are represented as SD. (For *mt-nd1*: p-
1000 value<0.05, for *mt-nd6*, *mt-cyb*, *mt-atp8*: p-value<0.01, for *mt-nd4*, *mt-co1*, *mt-atp6*: p-
1001 value<0.001, for *rps6kb1* and *nfe2l2a*: p-value –not significant).

1002 **Figure 4: *lrpprc* homozygous mutants display decreased birefringence. (A-B)** Representative
1003 Birefringence images of wildtype **(A)** and *lrpprc*$^{GBT0235/GBT0235}$ mutants **(B)**. **(C-E)** The images

1004 and graphs in the figure show the area of region of interest (ROI) **(C)**, mean gray value **(D)** and
1005 integrated density **(E)** between wild type and *lrpprc*$^{GBT0235/GBT0235}$ mutants of the birefringence
1006 signal. *lrpprc*$^{GBT0235/GBT0235}$ mutants display similar birefringence area but a decrease in mean
1007 gray value (p value<0.0001) and integrated density (p value=0.001). Each individual data point
1008 represents a single animal. Each parental pair represents biological replicate.

1009 **Figure 5: RNAseq of *lrpprc*$^{GBT0235/GBT0235}$ homozygous mutants. (A)** Volcano plot of
1010 differentially expressed genes in the homozygous mutants. Logarithm (base 2) of fold change is
1011 represented on the x-axis and logarithm of p-value (base 10) is represented on y-axis. Red dot
1012 signifies the significantly differentially expressed genes and black dots represent the non-
1013 significantly differentially expressed genes between the 6 days post fertilization homozygous
1014 *lrpprc*$^{GBT0235/GBT0235}$ and wild-type *lrpprc*$^{+/+}$ larvae. **(B)** Heat map visualization of expression of
1015 zebrafish orthologs for human Mitocarta genes. Gradient color scale represents the $\log_2$CPM
1016 value obtained for each of the zebrafish mitochondrial orthologs in the two data sets. **(C)**
1017 PANTHER classification for all the significantly differentially expressed genes in the
1018 homozygous mutant according to protein class and biological process. Each histogram represents
1019 the percentage of genes falling in each of the category.

1020 **Figure 6: Liver plays an important role in the pathology of LSFC and genetic liver specific**
1021 **rescue rescues the lipid defect and mortality in *lrpprc* homozygous mutant larvae. (A-B)**
1022 Representative images of the livers of 6 dpf old heterozygous (A) *lrpprc*$^{GBT0235/+}$and homozygous
1023 (B) *lrpprc*$^{GBT0235/GBT0235}$ mutants at 40X (Scale bar: 50 µm). **(C)** Brightfield image of 6 dpf wild
1024 type, *lrpprc*$^{+/+}$ and homozygous *lrpprc*$^{GBT0235/GBT0235}$ mutants. Homozygous mutants display dark
1025 liver phenotype as compared to the wild type controls. Region showing dark liver has been
1026 marked by asterisk. **(D-F)** Oil red O staining for assessment of lipid accumulation in the 8 dpf
1027 mutants and 8 dpf rescued larvae. Increased lipid accumulation was observed in the homozygous
1028 mutants **(E)** compared to wild type larvae **(D)**. In the liver-specific rescued homozygous *lrpprc*
1029 mutants *Tg(fabp10:Cre)lrprrc*$^{GBT0235/GBT0235}$, no accumulation of lipids was observed **(F)**. **(G)**
1030 The graph show increase in the area of region of interest (ROI) for the accumulated lipids,
1031 between wild type and *lrpprc*$^{GBT0235/GBT0235}$ mutants, indicating a decrease in the lipid content (p
1032 value < 0.05) (Scale bar; G-I: 20 px). The levels are restored in homzygous rescued larvae (p
1033 value < 0.05). **(H)** Liver -specific rescued mutants display an improved survival rate beyond 11
1034 dpf. **(I-L)** Representative electron micrographs of the mitochondria in hepatocytes for 8dpf

1035 lrpprc wild type **(I)**, *lrpprc* homozygous mutants (J) and liver-specific *lrpprc* rescued larvae **(K**
1036 **and L)**. Altered mitochondrial morphology displayed by *lrrprc*$^{GBT0235/GBT0235}$ (J) is improved in
1037 the rescued mutants, *Tg(fabp10:Cre)lrprrc*$^{GBT0235/GBT0235}$ (K and L) (Scale bar; A-C: 0.5 µm).

1038 **Figure 7: Genetic liver-specific rescue of altered dietary lipid metabolism in *lrpprc***
1039 **homozygous mutant larvae. (A-D)** HPLC studies reveal that *lrpprc* homozygous mutants have
1040 double the level of nonpolar lipids compared to their wildtype siblings. **(A)** Representative
1041 chromatographs are shown: lipid extractions from whole wildtype larvae (top) and whole *lrpprc*
1042 homzygous mutant larvae (middle). Peaks represent different lipid species and are quantified by
1043 peak area. Measuring the peak of the non-metabolizable fluorescent reagent (22–23 min elution
1044 time) confirms that the *lrpprc*$^{GBT0235/GBT0235}$ mutants ingest less than their wildtype siblings and
1045 provides a normalizer for the other measured peaks. Liver-specific rescue of *lrpprc*$^{GBT0235/GBT0235}$
1046 mutants restores nonpolar lipid levels to wildtype levels liver-specific rescued homozygous
1047 mutant larvae (bottom). All peaks were normalized to the peak marked by asterisk(*) reflecting
1048 non-metabolizable fluorescent reagent (amount ingested). **(B)** Levels of several nonpolar lipid
1049 species are higher in *lrpprc* homozygous mutants. Excerpts from representative chromatographs,
1050 wildtype larvae (top) and *lrpprc* homozygous mutant larvae (bottom); peaks shown have been
1051 normalized to account for amount ingested. Peaks or peak areas (labeled as 1-4) were
1052 individually analyzed for contribution to the overall higher NPL level in *lrpprc* homozygous
1053 mutants compared to their wildtype siblings. **(C)** 95% CI plot: *lrpprc*$^{GBT0235/GBT0235}$ generated
1054 2.04 times more non-polar lipids compared to their wildtype siblings
1055 (*lrpprc*$^{GBT0235/GBT0235}$/*lrpprc*$^{+/+}$ = 2.040, 95% CI = 1.122–3.709, p= 0.019). **(D)** 95% CI plot:
1056 *Tg(fabp10:Cre)lrprrc*$^{GBT0235/GBT0235}$ restored the levels of non-polar lipids as compared to
1057 *lrpprc*$^{GBT0235/GBT0235}$ homozygous mutants. PL=phospholipids; NPL=nonpolar lipids
1058 (triacylglycerides, diacylglycerides); CE=cholesteryl ester; NM=normalizer for amount eaten.

1059 **Figures:**

1060 **Figure 1:**

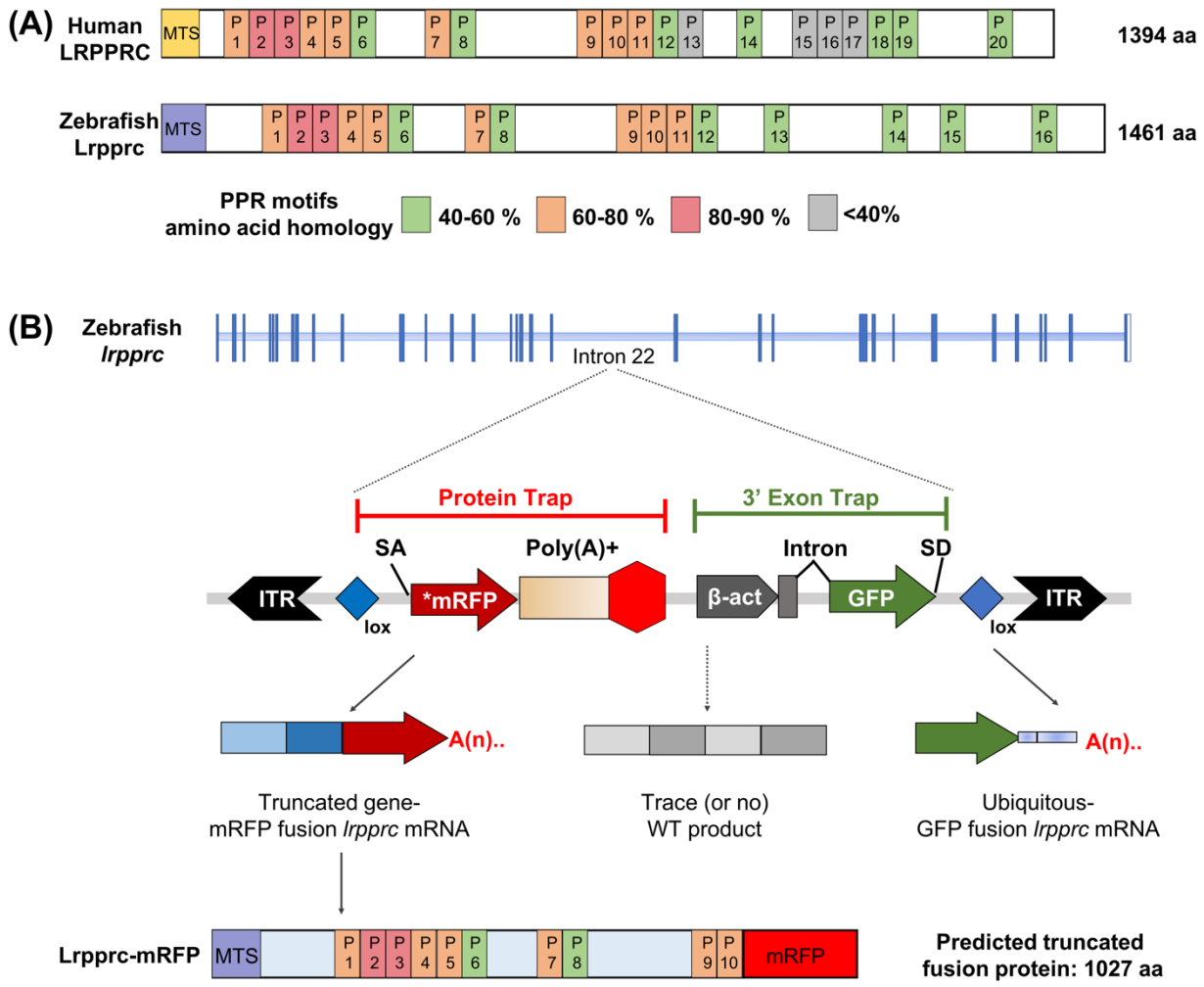

1061

1062

1063 **Figure 2:**

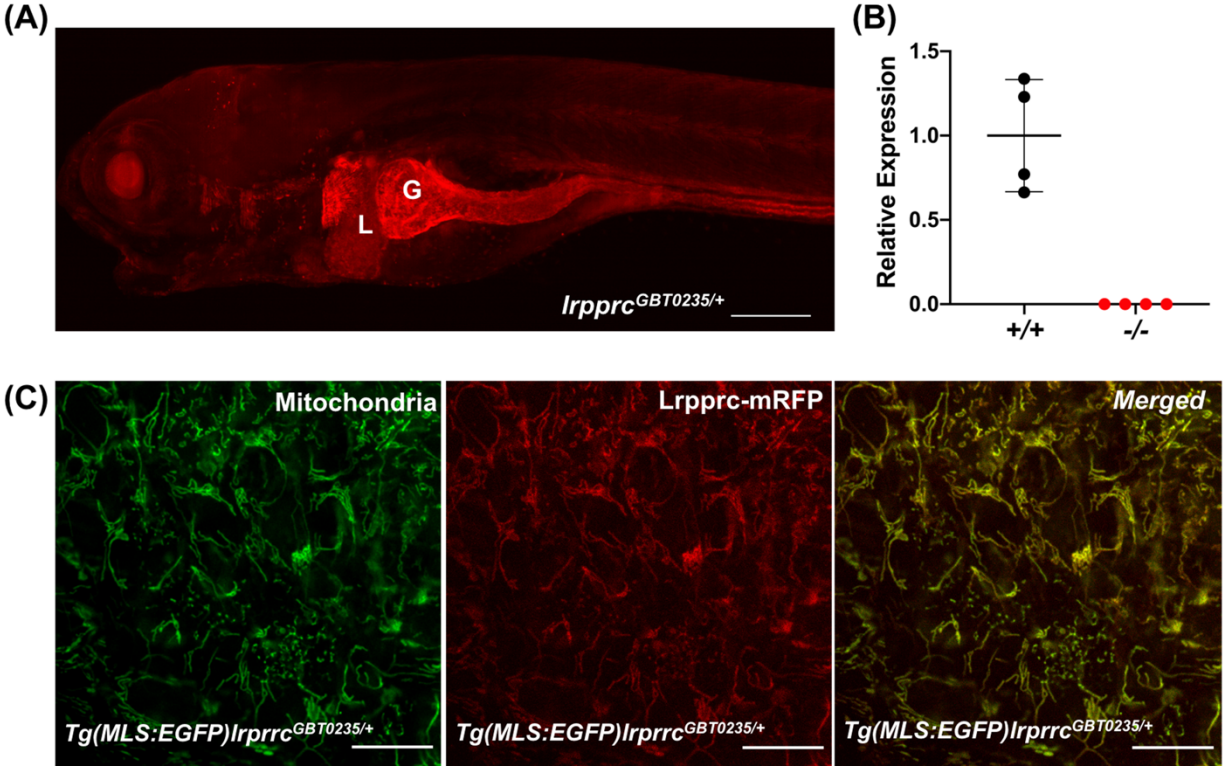

1064

1065 **Figure 3:**

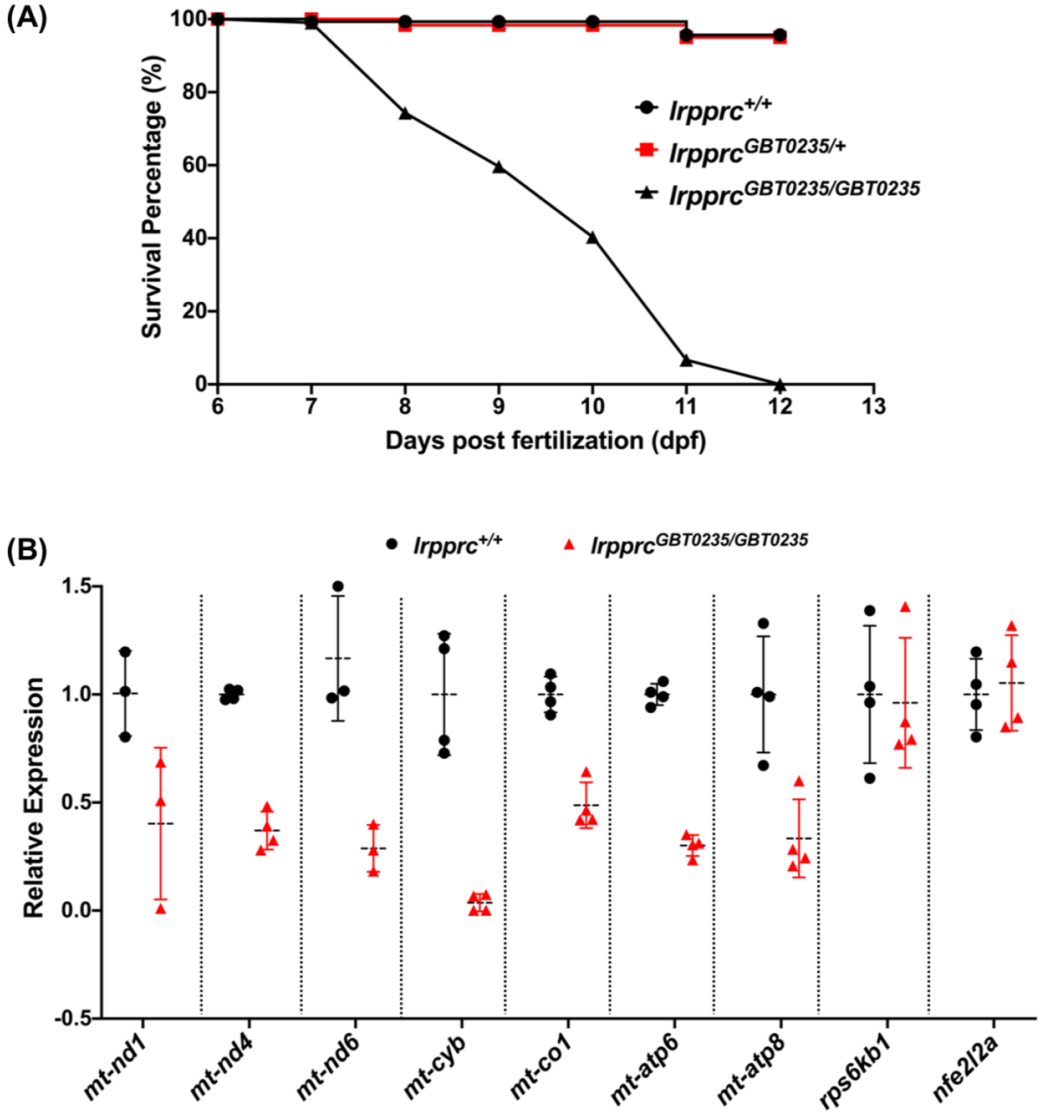

1066

1067 **Figure 4:**

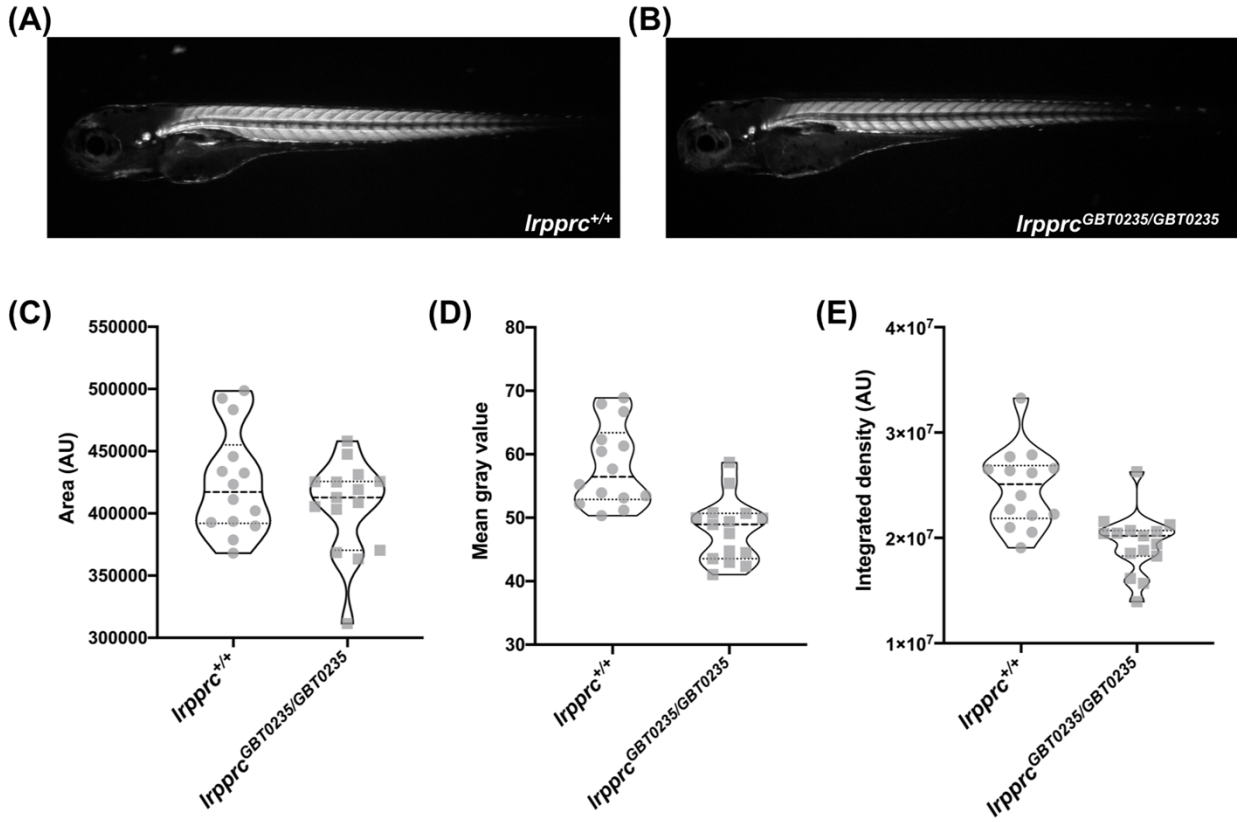

1068

1069 **Figure 5:**

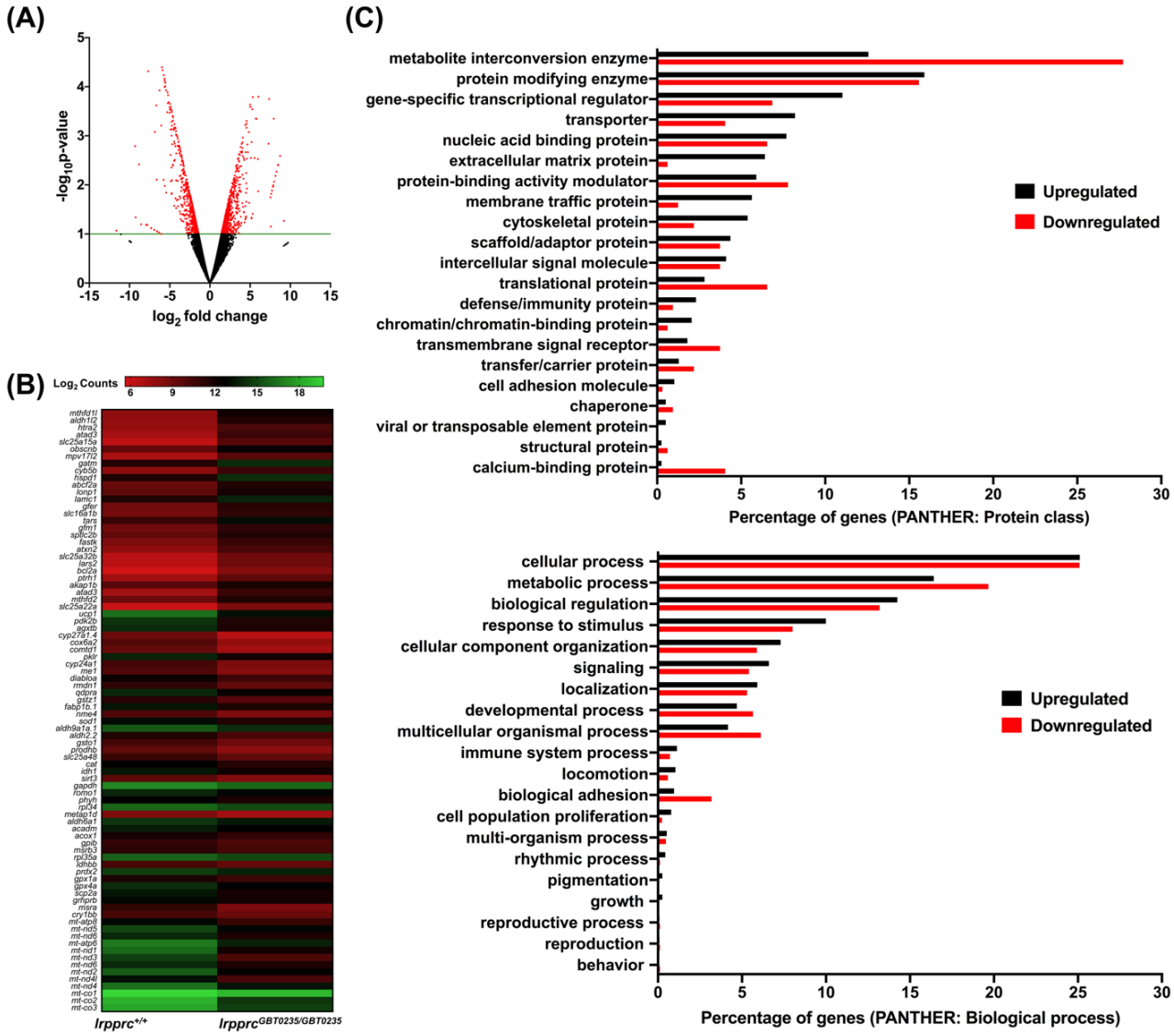

1070
1071

1072 **Figure 6:**

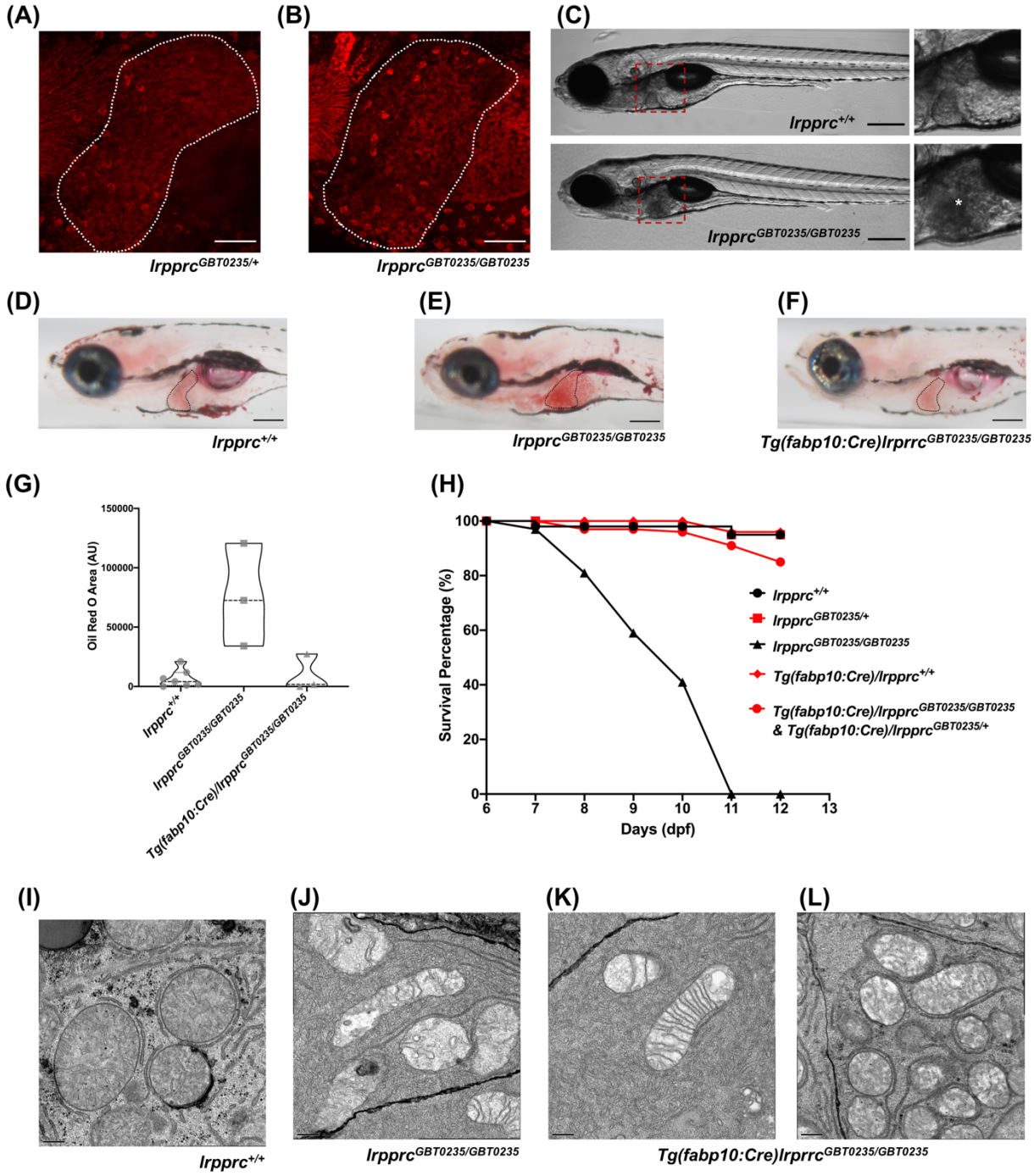

1073

1074 **Figure 7:**

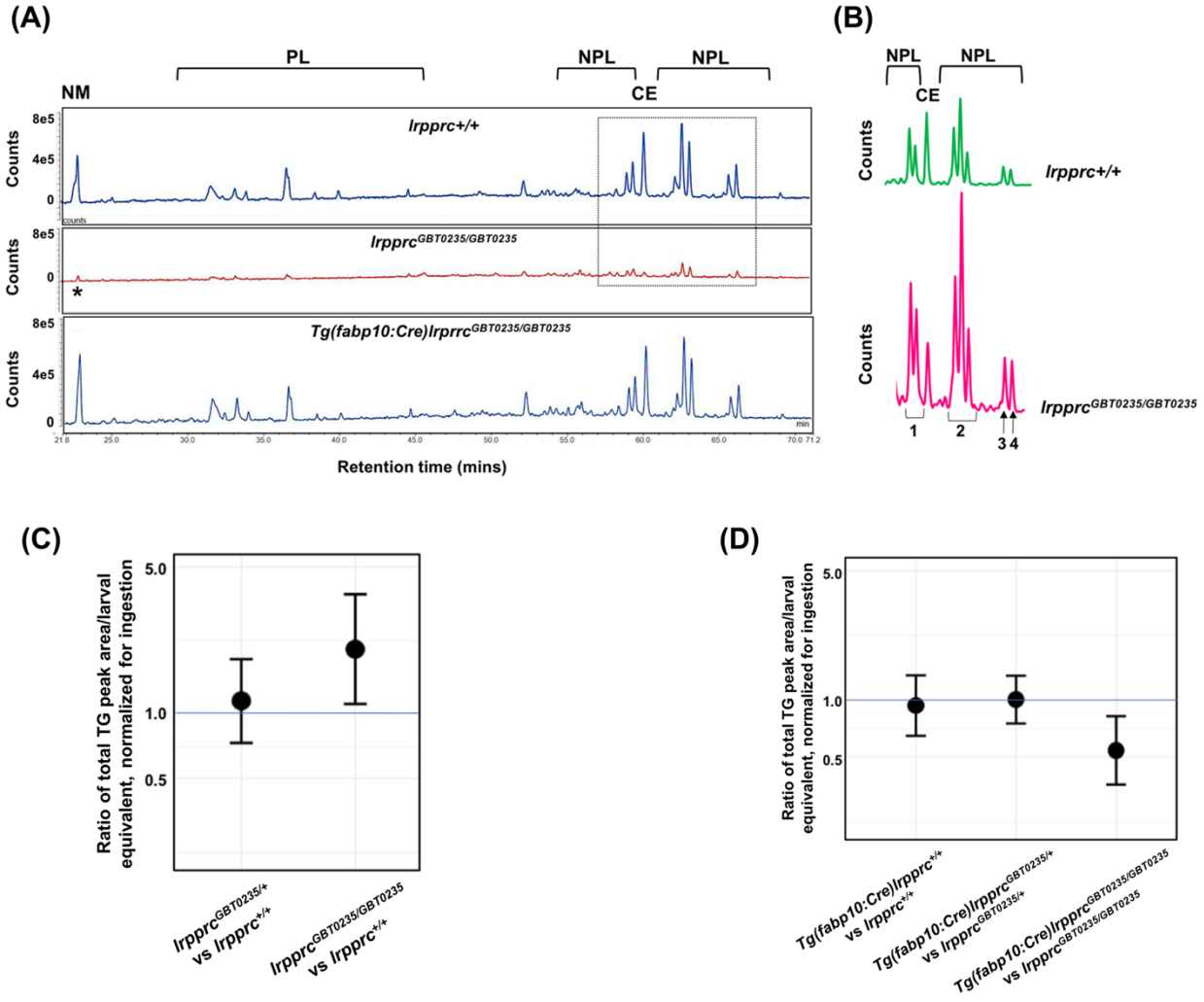

1075